1 # Assessing Locations Susceptible to Landslide Initiation During
2 # Prolonged Intense Rainfall in the Lares, Utuado, and Naranjito
3 # Municipios of Puerto Rico
4

5 Rex L. Baum[1], Dianne L. Brien[2], Mark E. Reid[2], William H. Schulz[1], and Matthew J. Tello[1,3]

6 [1]U.S. Geological Survey, Golden, Colorado 80401, USA[2]U.S. Geological Survey, Moffett Field, California 94035,
7 USA
8 [3]Present Address, Colorado Department of Transportation, Denver, Colorado 80204, USA

9 *Correspondence to*: Rex L. Baum (baum@usgs.gov)

10

11   **Abstract**. Hurricane María induced about 70,000 landslides throughout Puerto Rico, USA, including thousands each

12   in three municipalities situated in Puerto Rico's rugged Cordillera Central range. By combining a nonlinear soil-depth

13   model, presumed wettest-case pore pressures, and quasi-three-dimensional (3D) slope-stability analysis we developed

14   a landslide susceptibility map that has very good performance and continuous susceptibility zones having smooth,

15   buffered boundaries. Our landslide susceptibility map enables assessment of (1) potential ground-failure locations,

16   and (2) areas of potential landslide sources to support a companion assessment of inundation and debris-flow runout.

17   The quasi-3D factor of safety, F_3, showed strong inverse correlation to landslide density (high density at low F_3). Area

18   under the curve (AUC) of True Positive Rate (TPR) versus False Positive Rate indicated success of F_3 in identifying

19   head-scarp points (AUC=0.84) and source-area polygons ($0.85 \leq$ AUC ≤ 0.88). The susceptibility zones enclose

20   specific percentages of observed landslides. Thus, zone boundaries use successive F_3 levels for increasing TPR of

21   landslide head-scarp points, with zones bounded by F_3 at TPR=0.75, very high; F_3 at TPR=0.90, high; and the

22   remainder moderate to low. The very high susceptibility zone, with 118 landslides/km^2, covered 23% of the three

23   municipalities. The high zone (51 landslides/km^2) covered another 10%.

24   **1 Introduction**

25   Heavy rainfall from Hurricane María during September 2017 produced tens of thousands of landslides on the main

26   island of Puerto Rico, USA (Bessette-Kirton et al. 2017, 2019a; Hughes et al. 2019). Shallow, translational failures in

27   soil or saprolite, from decimeters to a few meters deep were the most common landslides. Deeper (up to 30 m) complex

28   failures in soil, saprolite, and rock, as well as rock falls and rock slides also occurred (Bessette-Kirton et al. 2017).

29   Many landslides transformed into debris flows that commonly coalesced and flowed down channels. Landslides

30   caused fatalities as well as widespread damage to homes, roads, and other infrastructure.

31   In the aftermath of the hurricane, the U.S. Geological Survey (USGS) began working with local partners to conduct

32   detailed assessments of landslide and debris-flow hazards, both island-wide (Hughes and Schulz 2020a, b) and more

33   locally (this study) for three impacted municipalities (Lares Municipio, Utuado Municipio, and Naranjito Municipio)

34   in the central mountains of Puerto Rico. Here we describe the landslide initiation (source area) part of a landslide

35   susceptibility assessment for these municipalities. Estimating landslide initiation potential is part of a larger effort (in

36   progress, Brien et al. 2021) to estimate overall hazard from (1) landslide initiation (ground failure), (2) landslide

37   runout, and (3) debris-flow inundation from future extreme rainfall, including tropical cyclones (hurricanes), as well

38   as localized storms expected to impact these areas of Puerto Rico.

39   One of the objectives of this work is to produce integrated maps of potential landslide initiation and inundation areas.

40   Although much progress has been made in methods for assessing landslide susceptibility (e.g., Carrara et al. 1999;

41   Chung and Fabri 2003; Lee et al. 2003; Godt et al. 2008; Baum et al. 2014; Canli et al. 2018) as well as debris-flow

42   inundation (George and Iverson 2014; Reid et al. 2016; Aaron et al. 2017; Bessette-Kirton et al. 2019b), combining

43   these two types of assessments into a single map for an area of hundreds of square kilometers remains challenging

44   (Ellen et al. 1993; Benda et al. 2007; Fan et al. 2017; Hsu and Liu 2019; Mergili et al. 2019). One of the challenges is

45   estimating potential source-area extent and depth. We addressed this challenge by modelling soil depth and using it to

46   approximate potential source-area depth in one-dimensional (1D) and quasi-three-dimensional (3D) slope stability

47 models for use in assessing regional shallow landslide susceptibility. Such an approach helps ensure that the
48 susceptibility model accounts for variable failure depth across the landscape and that predicted areas of potential
49 landslide sources are acceptable for use in assessing debris-flow inundation. The quasi-3D model uses a simplified
50 limit-equilibrium analysis to estimate the stability of a slab-shaped trial landslide. Another challenge is establishing
51 meaningful susceptibility categories, which we addressed by delimiting the categories at quasi-3D factor of safety
52 values, F_3, that enclose specific percentages of landslide sources, rather than relying on theoretical or arbitrary factor
53 of safety values to delimit the categories. By showing like outcomes (areas that capture specific percentages of
54 observed landslides), maps based on this approach are directly comparable to each other.
55 This study was conducted in stages between 2018 and 2022 and involved three study areas as well as calibration areas,
56 study-area tiles, and validation areas. We define these here to help the reader comprehend how our presentation of the
57 study is organized. The study areas comprise three municipalities, Lares Municipio, Utuado Municipio, and Naranjito
58 Municipio, and are the focus of our landslide initiation susceptibility maps (Supplemental Figures S1 and S2; Baum
59 et al. 2023). These municipalities were chosen because they were severely impacted by Hurricane María landslides
60 and to help manage their future growth and development. We enclosed the Lares and Utuado study areas in four
61 overlapping rectangles and enclosed Naranjito Municipio in a fifth, separate rectangle (Fig. 1a, 1b, and 1c). The
62 rectangles extend beyond the drainage divides of basins that straddle municipality boundaries. The rectangles delimit
63 overlapping tiles of the digital elevation models (DEM) used in the susceptibility analysis. These DEM tiles helped
64 keep file sizes (6 gigabytes or less for ASCII input and output grids) manageable and overlap ensured that edge effects
65 would not degrade soil-depth or slope-stability computations. The extended boundaries ensured that landslide runout
66 and debris-flow inundation models (Brien et al. in 2021) would not be impeded by municipality boundaries or other
67 artificial barriers. The calibration areas (Fig. 1) were placed in distinct geologic terranes where high concentrations of
68 landslides had occurred. Previous detailed mapping and characterization (Bessette-Kirton et al. 2019c, 2020) and field
69 studies (Baum et al. 2018) in these areas provided data for testing and calibrating soil-depth and slope-stability models
70 (Tello 2020). From east to west, each 2-km^2 calibration area was named for a nearby city: Añasco (ANA), Lares
71 (LAR), Utuado (UTU), and Naranjito (NAR). Although ANA is about 15 km west of the study areas, it was included
72 to provide additional calibration data in an area of high landslide density for submarine volcaniclastic lithologies
73 because sufficient data were not available at NAR. Soils, land cover, and other characteristics (besides bedrock
74 lithology) that influence landslide susceptibility vary between the four calibration areas (Bessette-Kirton et al. 2020;
75 Hughes and Schulz 2020a, 2020b). We used six additional areas of detailed mapping (Einbund et al. 2021a, 2021b) to
76 help evaluate the final maps. These validation areas are designated LAR2 and UTU2, and each includes three
77 rectangular areas of detailed landslide mapping. (Fig. 1b). We combined detailed source area mapping of NAR
78 (Baxstrom et al. 2021a) and UTU (Einbund et al. 2021a) with that in LAR2 and UTU2 for the validation.
79
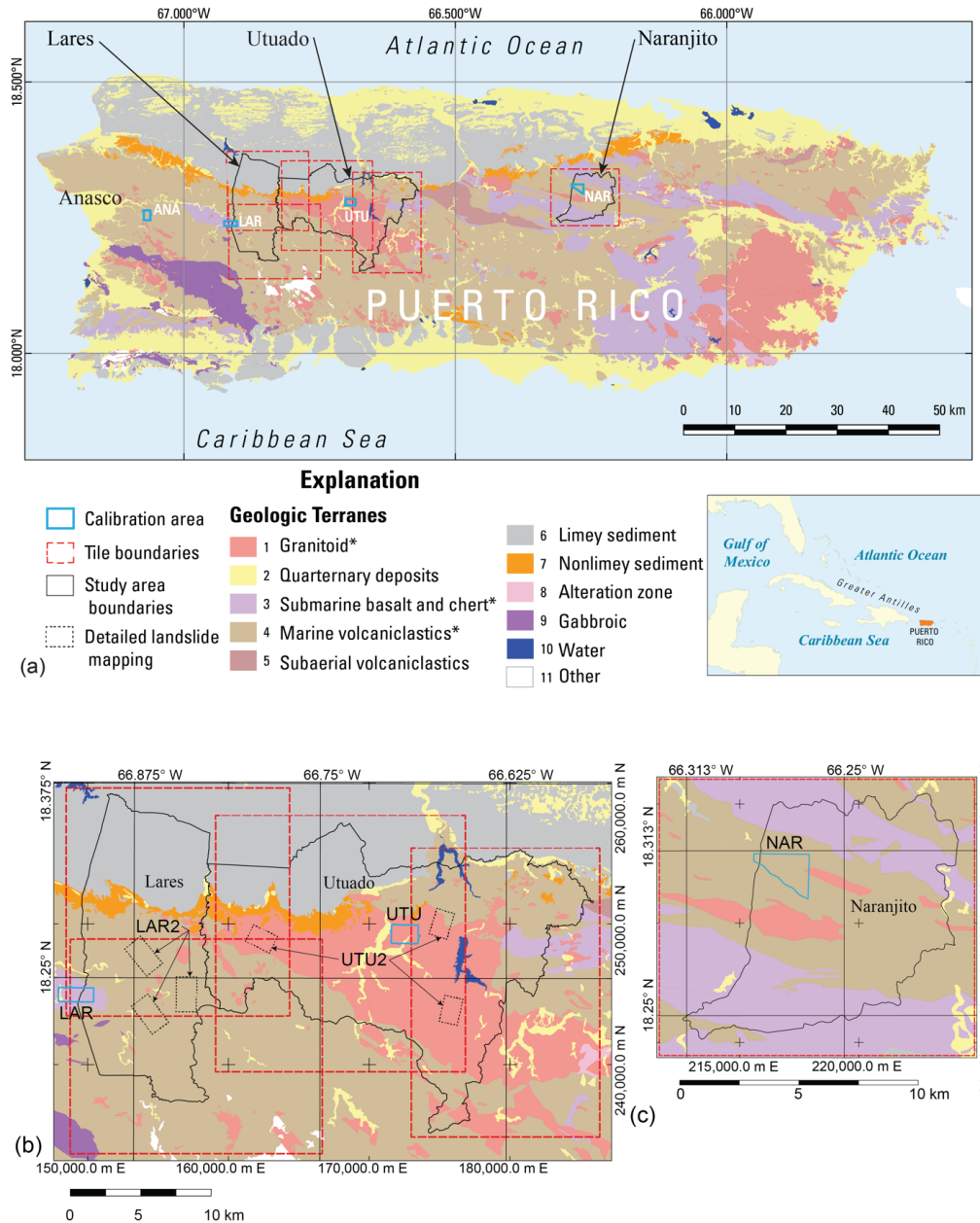
Figure 1. Geologic map showing municipality boundaries, study areas, calibration areas, and major lithologies (geologic terranes) for the main island of Puerto Rico. Simplified from Bawiec (1998) by combining submarine volcaniclastic rocks of various ages into a single map unit. Primary landslide-prone lithologies indicated by * in map explanation. Municipality boundaries of Lares, Utuado, and Naranjito define study areas. Digital elevation models covering the study areas were divided into five smaller tiles. Extent of Añasco (ANA), Lares (LAR), Utuado (UTU), and Naranjito (NAR) calibration areas from Bessette-Kirton et al. (2019c, 2020). (a) overview of entire island, (b) details of Lares and Utuado study areas including outlines of areas of detailed landslide mapping in Utuado, (UTU2, Einbund et al. 2021a) and Lares (LAR2, Einbund et al. 2021b), (c) details of Naranjito study area.

89   In the following sections, we describe characteristics of the study areas, summarize our methods and results, and

90   discuss advantages, limitations, and implications of our approach. First, we describe the setting, geology, and

91   landslides of Puerto Rico including details specific to the study areas. Then we describe the available topographic and

92   geotechnical data followed by a description of the workflow for assessing landslide susceptibility. Next, we describe

93   our methods for modelling soil depth, pressure head, and slope stability along with procedures for model calibration

94   and details of how the calibrated models were applied to and evaluated for our study areas. Then we present results of

95   the calibration, soil-depth modelling, 1D and quasi-3D stability analyses, and the evaluation and validation of the

96   susceptibility analysis. These results were obtained using pre-event light detection and ranging (lidar) DEMs (U.S.

97   Geological Survey, 2018); we reran our models using calibrated input parameters and post-event lidar (U.S.

98   Geological Survey 2020a, b, c) to estimate susceptibility to future landslides. We finish by discussing strengths and

99   limitations of our approach as well as some unexpected findings and ways to simplify the workflow for application to

100   areas where limited data are available.

2 Study area

102   Puerto Rico is a U.S. territory and lies at the east end of the Greater Antilles island chain in the Caribbean Sea (Fig.

103   1). The main island is characterized by rugged topography and covers an area of 8750 km^2. The study areas and

104   calibration areas lie in the east–west-trending Cordillera Central range, which spans most of the island. The range

105   exceeds elevations of 900 m at many places, and its highest peak reaches an elevation of 1340 m. Coastal plains and

106   broad lowlands ring most of the island. Ongoing tectonic uplift is one of the main factors creating the rugged

107   topography across the island (Taggart and Joyce 1991). Warm temperatures, high rainfall, and humidity contribute to

108   deep weathering and widespread saprolite formation (Murphy et al. 2012).

2.1 Geology and soils

110   Heavily faulted basement rocks, consisting mainly of oceanic crust, volcaniclastic, and intrusive rocks, underlie the

111   Cordillera Central range (Jolly et al. 1998). A cover sequence of carbonates and associated clastic sediments

112   unconformably overlies the basement complex. The carbonates have weathered to form tropical karst in the lowlands

113   north of the range (Monroe 1976). Bawiec (1998) generalized the geology of Puerto Rico into twelve geologic terranes

114   having related rock types. We have simplified the terranes slightly for purposes of this study (Fig. 1). Soil mapping

115   and databases published by the U.S. Department of Agriculture's Natural Resources Conservation Service (NRCS)

116   indicate a wide range in the textures (particle-size distributions) and hydraulic properties of soils in the study areas

117   (Soil Survey Staff 2018). Most hillside soils have developed by in-place chemical weathering of underlying bedrock

118   or saprolite and locally derived colluvium. Despite the steep slopes, in many places the upper few meters of bedrock

119   have weathered to saprolite (e.g., Jibson 1989; Larsen and Torres-Sanchez 1992).

2.2 Landslides

121   Recent and historical studies described and characterized Puerto Rico's rainfall-induced landslides. Published studies

122   of past landslides characterized rainfall-induced landslides in southern and eastern parts of Puerto Rico (Jibson 1989;

123   Simon et al. 1990; Larsen and Torres-Sanchez 1992, 1998; Pando et al. 2005; Larsen 2012). Several post-Hurricane

124   María studies documented dimensional, geologic, and topographic characteristics of landslide sources in ten

125   representative areas of high landslide density within and near the municipality study areas (Fig. 1): Baum et al. (2018)

126   conducted field studies and measurements (Fig. 2), and Bessette-Kirton et al. (2019c) later mapped landslides using

127   post-event aerial photography in the four areas denoted as ANA, LAR, NAR, and UTU (Fig. 1a). U.S. Geological

128   Survey staff later remapped NAR (Baxstrom et al. 2021a), remapped UTU (Einbund et al. 2021a), and mapped six

129   additional areas (UTU2 and LAR2, Fig. 1b) near UTU and LAR (Einbund et al. 2021a, 2021b). Schulz et al. (2023)

130   expanded on earlier field studies of Baum et al. (2018). Data from some of these studies supported recent analyses of

131   landslide susceptibility (Bessette-Kirton et al. 2019a; Hughes and Schulz 2020a) and runout characteristics (Bessette-

132   Kirton et al. 2020).

133

134
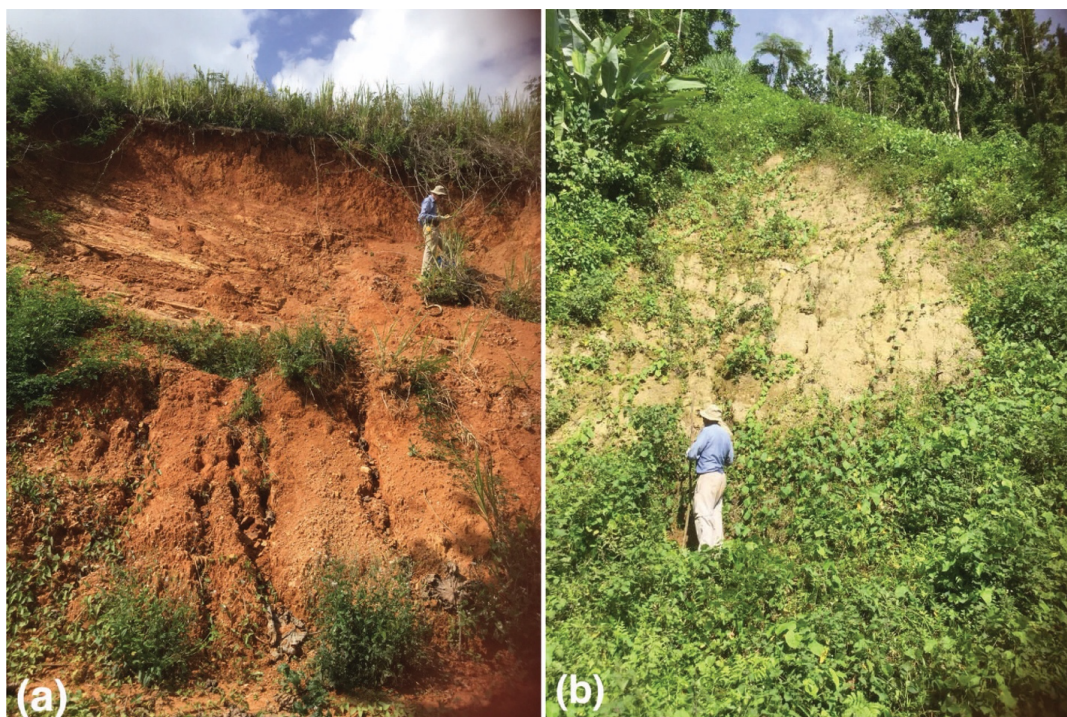
Figure 2. Photographs taken in May 2018 depicting source areas of shallow landslides in (a) volcaniclastic terrane and (b) granitoid terrane eight months after Hurricane María (photographs by C. Cerovski-Darriau, U.S. Geological Survey, public domain).

138   The post-Hurricane María studies cited above indicated that most source areas were fully evacuated, and shallow

139   translational slides appear to be the most common type of movement prior to transforming to debris flows.

140   Nevertheless, source area shapes were consistent with translational, rotational, or complex movement. Source areas

141   exposed soil, saprolite, and bedrock (Fig. 2). Soil matrix textures ranged from sand to clay; clast content increased

142   with depth. Differences between the landslide source sizes and depths within the different terranes (Fig. 3) seem

Natural Hazards
and Earth System
Sciences
Discussions
Open Access
EGU

143 consistent with their different lithologies and depth of weathering (volcaniclastic rocks, weathered volcanic rocks,

144 granitic pluton).

145

146
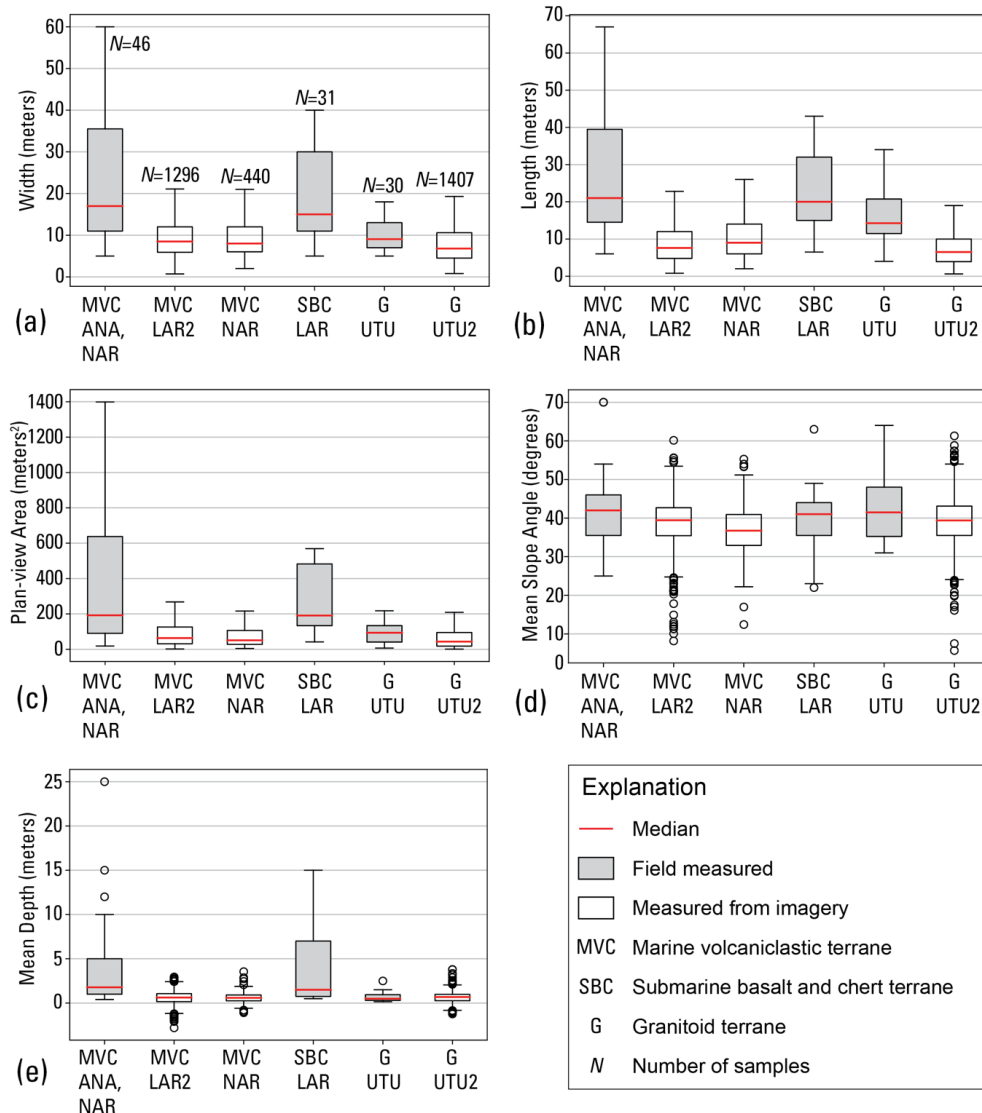
Figure 3. Box plots summarizing landslide source dimensions obtained for three geologic terranes by field studies of 107
landslides (gray, Baum et al. 2018) and by mapping 3440 landslides from aerial imagery and lidar-derived digital elevation
models (white, Baxstrom 2021a; Einbund 2021a, 2021b). (a) width, (b) length, (c) plan-view area calculated directly by
geographic information system for mapped polygons and estimated from field measurements as an ellipse and projected to
the horizontal, $\pi \times$ (Length × Width × cos (Slope angle))/4, (d) mean slope angle, (e) mean landslide source depths. Outliers
of width, length and area not shown to keep 25%, 50%, and 75% quartiles legible. [Locations (as shown in Fig. 1): ANA,
Añasco; LAR, Lares; LAR2, Lares (Einbund et al. 2021b); UTU, Utuado; UTU2, Utuado (Einbund et al. 2021b, includes
UTU); NAR, Naranjito (remapped by Baxstrom et al. 2021a)].

155   Figure 3 summarizes landslide dimensions obtained from the post-Hurricane María studies for the three main geologic

156   terranes in the study areas (Fig. 1). The field measurements (using laser range finder, tape, and clinometer; Baum et

157   al. 2018), though biased by purposely including several large landslides (1500 m^2 – 6600 m^2), represent the range of

158   sizes of Hurricane María landslide sources. Mapping from imagery (Baxstrom et al. 2021a; Einbund et al. 2021a,

159   2021b) included all landslides visible in the imagery of several 2.5-km^2 target areas and represent typical dimensions

160   of landslides triggered by the hurricane on uplands and valley side slopes. Most landslide sources had lengths and

161   widths less than 10-15 m, with median mapped length and width among the different samples in Figure 3a, 3b ranging

162   from 6.5 m to 9 m. Many landslide sources have areas less than 100 m^2 (median mapped areas range from 42 m^2 to

163   64 m^2 for the different terranes), and very few have areas greater than 1000 m^2 (Fig. 3c). Although landslides occurred

164   on a wide range of slope angles, most occurred on slopes between 30º and 50º (Fig. 3d). Median DEM-derived slope

165   angles of mapped landslide sources were 37° - 39° (Fig. 3d). Depths computed by differencing pre-event and post-

166   event lidar elevation data (Baxstrom et al. 2021a; Einbund et al. 2021a, 2021b) have significant uncertainty because

167   14 - 19% of the landslide sources had mean and median elevation differences indicating net gain of material (Fig. 3e).

168   In addition, undisturbed areas outside the landslide polygons showed elevation differences that varied horizontally,

169   which is consistent with alignment errors between the pre- and post-event lidar. However, it seems unlikely that any

170   of the mapped landslides had a mean depth much greater than 5.8 m (the span between the greatest elevation loss and

171   gain, MVC/LAR2, Fig. 3e). Rare, large landslides had depths as great as 25 m according to field measurements (Fig.

172   3e).

173   Puerto Rico's complex geology (Fig. 1), tropical soils, rugged terrain, land use, and landcover exert strong influences

174   on landslide susceptibility. Lepore et al. (2012) in an island-wide assessment using frequency ratio and logistic

175   regression concluded that aspect, slope, elevation, geological discontinuities, and geology, were "highly significant

176   landslide-inducing factors;" land cover and distance from roads were also significant. Bessette-Kirton et al. (2019a)

177   showed that antecedent soil moisture was statistically correlated to densities of Hurricane-María-induced landslides

178   and found that high landslide densities were "especially widespread across some geologic formations," although the

179   degree to which rainfall characteristics resulted in this correlation remained unclear. In a later post-Hurricane María,

180   island-wide assessment using the frequency ratio method, Hughes and Schulz (2020a) found after accounting for the

181   effects of soil moisture, there were strong correlations between landslides and slope, curvature, geologic terrane, mean

182   annual precipitation, land cover, soil type, event soil moisture, proximity to roads, and proximity to fluvial channels

183   for the Hurricane María event. Previous, more localized studies considered fewer geomorphic and geographic

184   characteristics to classify landslide susceptibility using empirical and statistical methods (Larsen and Parks 1998;

185   Larsen et al. 2004). For example, Larsen and Parks (1998) classified landslide susceptibility of Comerío Municipality

186   based on elevation, slope, aspect, and land use. Our current study uses physics based geotechnical models of slope

187   stability to directly assess topographic, geologic, and soil controls on landslide potential and to indirectly assess effects

188   of roads and land use through their impacts on topography and surface drainage as expressed in the DEM as local

189   changes in the slope characteristics.

Natural Hazards
and Earth System
Sciences
Discussions

Open Access

EGU

190   **3 Methods and materials**

191   **3.1 Topographic data**

192   In 2015 and 2016, the U.S. Geological Survey (2018) acquired airborne lidar covering the entire main island of Puerto

193   Rico. These data were processed to create a 1-m resolution bare-earth DEM. Referred to hereafter as pre-event lidar,

194   these data were acquired roughly one to two years before Hurricane María and constitute the best available

195   representation of topographic conditions before the landslides associated with the hurricane occurred. Available at the

196   beginning of our investigation, the pre-event lidar-derived DEMs have formed the topographic mainstay for U.S.

197   Geological Survey studies of these recent landslides. We used these data for calibration and validation of our soil

198   depth and slope stability models. After Hurricane María, the U.S. Geological Survey (2020a, b, c) acquired additional

199   lidar data covering the entire island in 2018. These data, referred to hereafter as post-event lidar, constitute the

200   (currently) best available representation of topographic conditions after the landslides and are useful for assessing

201   susceptibility to future landslides. The 0.5-m post-event lidar DEMs were resampled to 1-m resolution for consistency

202   with the pre-event lidar and computational efficiency of landslide susceptibility models. We used these post-event

203   DEMs to run our models (using the previously calibrated and evaluated input parameters) to obtain our best estimate

204   of susceptibility to future landslides.

205   **3.2 Data compilation**

206   Based on findings by Bessette-Kirton et al. (2019a) and Hughes and Schulz (2020a, b) indicating strong correlation

207   between landslide density and both bedrock and soil type, Baum (2021) compiled existing data on soil texture and

208   engineering properties to create typical values for model calibration. Four different sources yielded soil and (or)

209   engineering data: published literature about past and recent landslides in Puerto Rico (Sowers 1971; Jibson 1989;

210   Simon et al. 1990; Larsen and Torres-Sanchez 1992, 1998; Lepore et al. 2013; Thomas and Cerovski-Darriau 2019),

211   NRCS soil databases (Soil Survey Staff; 2018), laboratory testing (Smith et al. 2020), and geotechnical reports of

212   recent landslides (Puerto Rico Department of Transportation, written commun. 2019). The NRCS soil data and

213   geotechnical reports were summarized in spreadsheets and then analyzed to determine means, ranges, and other basic

214   statistics to characterize the properties of soils and geologic formations found throughout the three municipalities

215   (Baum and Lewis, 2023). Baum (2021) identified dominant soil classes of the geologic terranes that had high landslide

216   densities (Fig. 1) and estimated expected ranges of soil strength parameters, cohesion, c', and angle of internal friction,

217   ϕ', both for effective stress based on dominant Unified Soil Classification System (ASTM International, 2020) types

218   in each terrane as follows: volcaniclastic, high-plasticity organic clay (OH), ϕ' 17º – 35º , c' 5 – 20 kPa; submarine

219   basalt and chert, low plasticity clay (CL) and high-plasticity silt (MH), ϕ' 27º – 35º , c' 5 – 20 kPa; granitoid, low

220   plasticity clay (CL) and silty sand (SM), ϕ' 27º – 41º , c' 0 – 20 kPa.

221   **3.3 Strength parameter analysis**

222   Using 1D slope stability analysis, Baum (2021) estimated the ranges of soil strength parameters φ' and c' that explain

223   the largest number of field-observed landslide slope and depth combinations in the calibration areas (Fig. 4).

224   Computing 1D factor of safety, F_1, for 1440 possible incremental combinations of ϕ' and c' over a synthetic grid in

225   which slope angle, δ, and landslide depth, H, varied incrementally over the observed ranges of slope ($22° - 60°$, in

226    $0.5°$ increments) and depth (0.2 m $-$ 15 m, in 0.1-m increments) produced F_1 values for more than 1.9×10^7

227   combinations of H, δ, ϕ', and c'. The best fitting ranges (dark red in Fig. 5) included combinations of H, δ, ϕ', and c',

228   where more than 75% of observed landslide scarp points were successfully predicted by $F_1 \geq 1$ for $\psi=0$ (dry, where ψ

229   is the pressure head at the basal slip surface) and $F_1 < 1$ for $\psi = H\cos^2\delta$ (water table at the ground surface with slope-

230   parallel flow). The example depicted in Fig. 4 had an overall success rate of 93% for its $c' - \phi'$ combination ($c' = 0.75$

231   kPa and $' = 54°$) in all three geologic terranes (Figs. 1, 5a). Compiling the performance of every c'-ϕ' pair considered

232   in the analysis led to Fig. 5b, 5c, and 5d, which showed the better-performing ranges of c' and ϕ' for the granitoid (Fig.

233   5b), volcaniclastic (Fig. 5c), and submarine basalt and chert (Fig. 5d) terranes, respectively. Those combinations of c'

234   and ϕ' with success rates exceeding 75%, were used as inputs for computing F_1 with trial soil-depth maps in subsequent

235   calibration studies to select a single combination of c' and ϕ' for computing F_1 in each terrane.

236

Natural Hazards
and Earth System
Sciences

Discussions
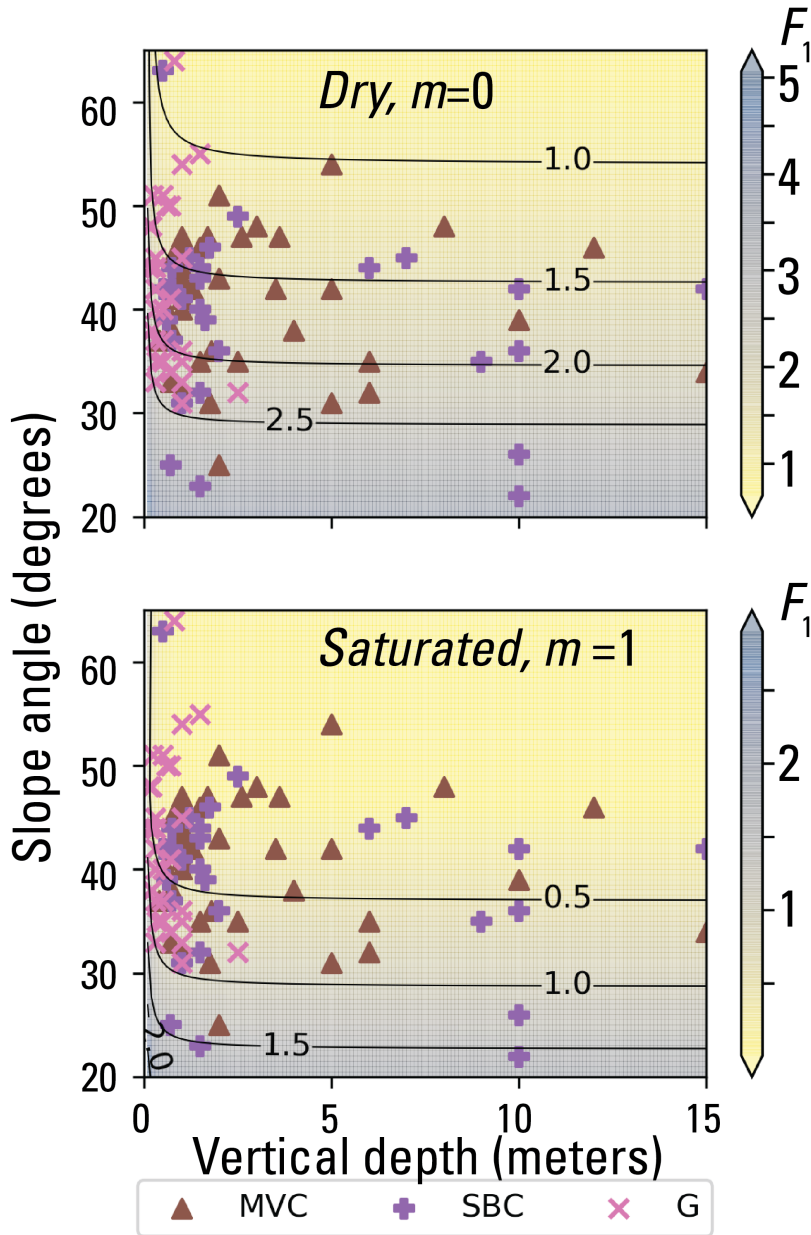
Figure 4. Results of strength parameter testing for observed combinations of landslide slope and depth in three geologic terranes. Factor of safety, F_1, results (indicated by color scale and contour lines) for a selected combination of cohesion, c' ($c' = 0.75$ kPa) and angle of internal friction, ϕ' ($\phi' = 54°$), both for effective stress. Two scenarios for pore-pressure head ($m=0$ and $m=1$) are shown, where m is the ratio of pressure head to soil depth. Symbols mark observed slope angle and depth at mapped landslide sources in various geologic terranes (Fig. 1). Factor of safety, F_1, at slope and depth combinations observed at marked landslide sources indicates model success ($F_1<1$ if $m=1$) or failure ($F_1>1$ if $m=1$). For the pair of c' and ϕ' values shown, $F_1>1$ for dry conditions ($m=0$) at about 97% of sources and $F_1>1$ at 4% of sources for water table at the ground surface with flow parallel to the slope ($m=1$). These parameters, $c' = 0.75$ kPa and $\phi' = 54°$, had an overall success rate of about 93% (=97% - 4%) for all three terranes (revised from Baum 2021).

247
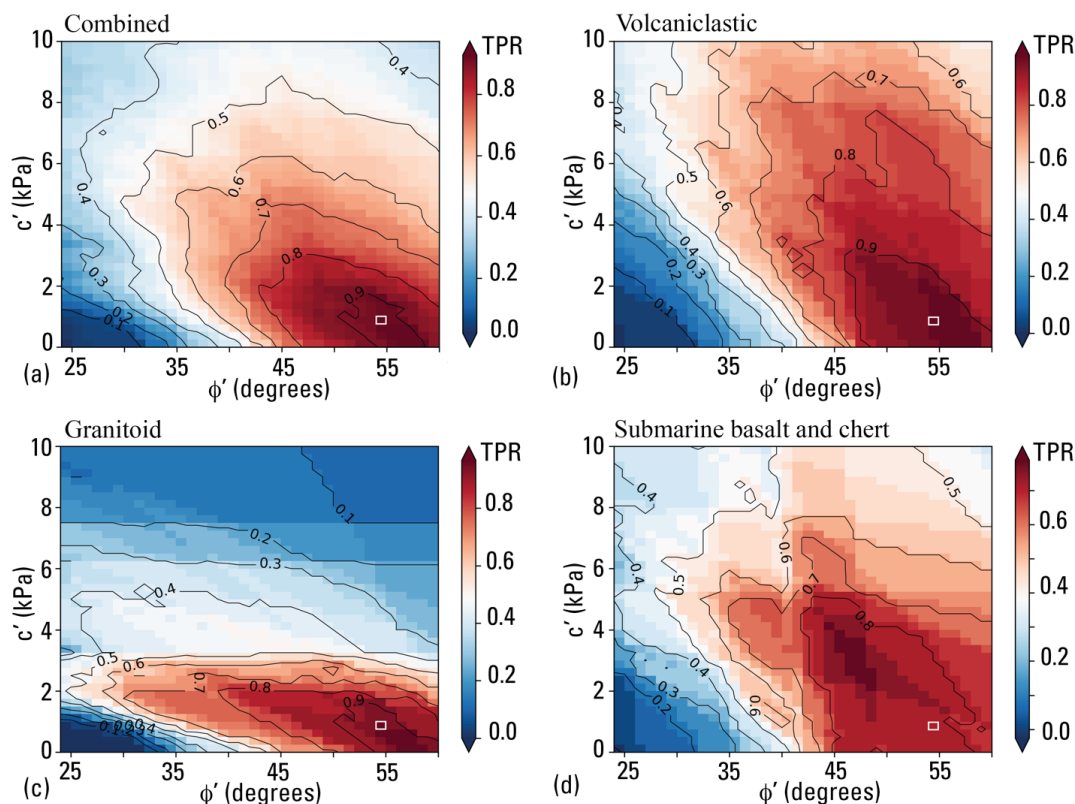
Figure 5. Fraction of field-measured landslide sources from the calibration areas (Baum et al. 2018) predicted correctly as a function of cohesion, c', and angle of internal friction, ϕ', for observed landslides in (a) all three terranes combined (modified from Baum 2021); (b) the volcaniclastic terrane; (c) the granitoid terrane; (d) the submarine basalt and chert terrane. Each pixel summarizes the net result of a pair of analyses like that in Figure 4. Pixel outlined by white rectangle in lower right corner of panels (a), (b), (c), and (d) indicates combination for analysis shown in Figure 4. Pixel color and contours indicate true positive rate (TPR) of predictions for each cell. Factor of safety for dry conditions is $F_{1m=0}$; factor of safety for water table at ground surface with slope-parallel flow is $F_{1m=1}$. Each grid cell represents the fraction $(NF_{1m=0} - NF_{1m=1})/N_t$, where $NF_{1m=0}$ is the number of source areas for $F_1 \geq 1$, $NF_{1m=1}$ is the number of source areas for which $F_1 \geq 1$, and N_t is the number of source areas in the geologic terrane.

3.4 Workflow for shallow landslide susceptibility models

To represent the aerial extent and depths of potential landslide source areas, we undertook a multistage process to calibrate and model potential landslide sources for both pre-Hurricane María and post-Hurricane María digital topography (Fig. 6). Each stage (depicted as a column in Fig. 6) repeated four distinct modelling steps: (1) soil depth, H, (2) pressure head, ψ, (3) 1D factor of safety, F_1, (4) quasi-3D factor of safety, F_3. The landscapes of the calibration and study areas were represented digitally in the models as raster grids based on 1-m-resolution pre-event lidar-derived DEMs. Each grid cell represented a column of potential landslide material of vertical depth, H, determined at soil-depth modelling steps A.1, B.1, and C.1 (Fig. 6). Computed soil depth from these steps became input for calculation of ψ, (steps A.2, B.2, and C.2, respectively, Fig. 6); then H and ψ became inputs for computing F_1 (steps A.3.a, B.3,

Natural Hazards
and Earth System
Sciences
Discussions

Open Access

EGU

267 and C.3, Fig. 6) and F_3 (steps A.4, B.4, and C.4, Fig. 6). F_1 was used primarily in evaluating soil-depth models and

268 shear-strength parameters for the calibration areas depicted in Fig. 1 using receiver operating characteristic (ROC)

269 analysis (step A.3.b, Fig. 6). During post-calibration slope-stability modelling of the study areas (steps B.4 and C.4,

270 Fig. 6), F_1 served as a rough check on the computed value of F_3. In this section (Sect. 3.4.1, 3.4.2, 3.4.3, and 3.4.4),

271 we briefly describe the modelling steps and give details about the models. We describe the major stages (columns in

272 Fig. 6) of calibration, modelling, and validation in later sections (Sect. 3.5, …, 3.11).

273
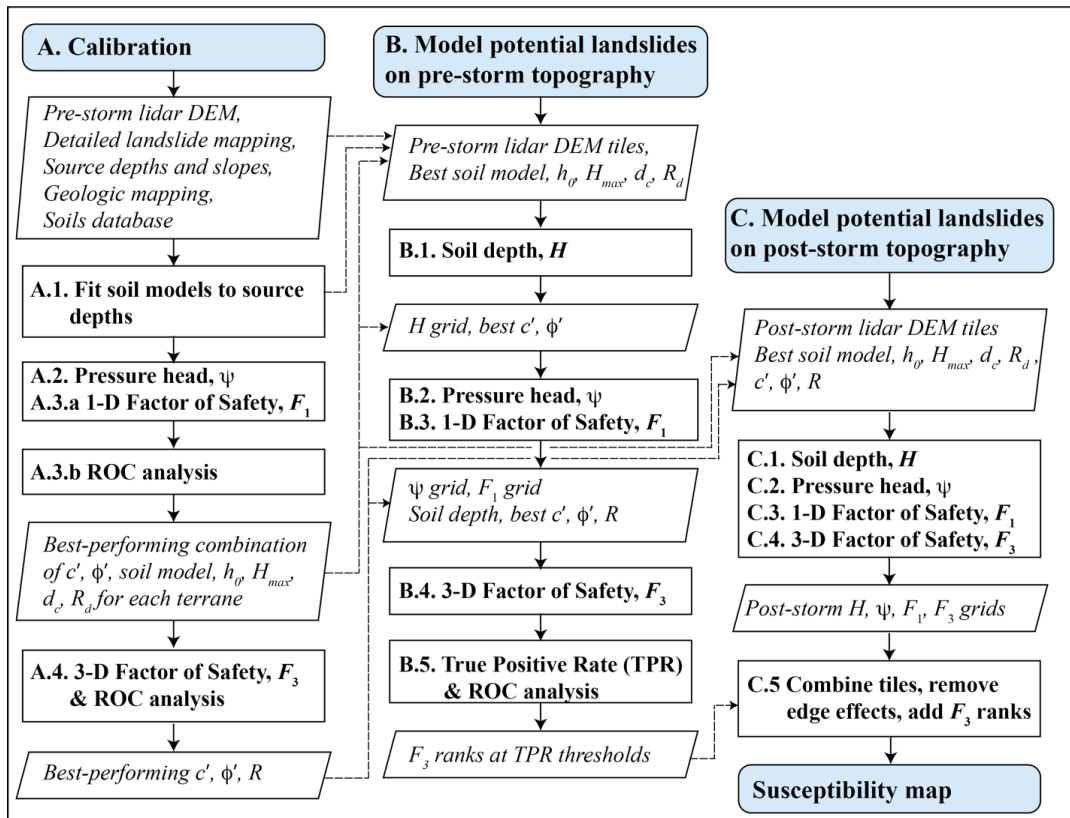
274

275 **Figure 6. Flow chart showing major stages (each column) and steps of calibration and modeling leading to the map of**
276 **landslide initiation susceptibility (Susceptibility map, bottom of right column). The calibration stage (left column) was**
277 **performed using digital elevation models of roughly 2.5-km² areas where detailed mapping and fieldwork had been**
278 **conducted (Fig. 1). Landslide source depths approximated soil depth for soil-depth model calibration (1.1). The pre-**
279 **Hurricane María (pre-storm) modeling stage (center column) was conducted using overlapping DEM tiles (Fig. 1) derived**
280 **from pre-Hurricane María lidar (U.S. Geological Survey, 2018). The post-Hurricane María (post-storm) modeling stage**
281 **(for generating map of future landslide susceptibility, right column) used overlapping DEM tiles (Fig. 1) derived from post-**
282 **Hurricane María lidar (U.S. Geological Survey, 2020a, b, c). Post-Hurricane María steps 3.1, 3.2, 3.3, and 3.4 used identical**
283 **input parameters to the corresponding pre-Hurricane María steps, 2.1, 2.2, 2.3, and 2.4. [Chart symbols: Light-blue**
284 **rounded rectangles, terminals of each major stage; rectangles with bold text, computational processes; parallelograms with**
285 **italic text, inputs or outputs; dashed lines, connections between calibration outputs and model inputs. Model outputs:** H,
286 **soil depth;** ψ, **pressure head;** F_1, **1D factor of safety;** F_3, **quasi-3D factor of safety; TPR, true positive rate; ROC, Receiver**
287 **Operating Characteristics. Model input parameters:** h_0, **characteristic soil depth,** H_{max}, **maximum soil depth;** δ_c, **critical**
288 **slope angle;** R_d, **diffusivity ratio;** c', **cohesion for effective stress;** ϕ', **angle of internal friction for effective stress;** R, **radius**
289 **of quasi-3D trial surface.]**

3.4.1 Step 1, modelling soil depth

Estimating soil depth from a DEM was the first modelling step in all three stages (Fig. 6). Field observations indicated that the base of most landslide sources occurred near the top of weathered bedrock (Baum et al. 2018; Baum 2021), so we chose soil depth as a predictor of landslide source depth. We carried out soil-depth estimation using new open-source software, REGOLITH (Baum et al. 2021) containing five empirical and four steady-state process-based soil-depth models implemented in a command-line program. Each model in REGOLITH estimates soil depth from some combination of topographic variables, including slope, upslope contributing area, and curvature, as well as a few model parameters, such as characteristic depth (the soil thickness at which bedrock lowering falls to 1/e of its maximum value), h_0 [L]; critical slope (angle of stability at which the slope is capable of transporting the entire soil profile by mass movement), δ_c [degrees]; and the ratio of maximum bedrock lowering rate to hillslope diffusivity, R_d. These parameters may vary with conditions that influence soil formation, including bedrock and climate. Predicted soil depth is treated as equivalent to and defines column height, H, in subsequent modelling steps. We used separate property zones with distinct parameters in REGOLITH to model adjoining areas of significantly different soil depth characteristics (tropical karst versus granitoid and volcaniclastic). We modified steady-state process-based models (Pelletier and Rasmussen 2009), which predict soil depth only on convex topography, to estimate soil depths in both concave and convex topography. We used a smoothing algorithm available in REGOLITH to reduce abrupt changes in soil depth that may result from DEM roughness. Further details are available in the online documentation found in the code repository (Baum et al. 2021). Our soil-depth, pressure head, and slope-stability models treated roads, cut slopes and embankments the same as other areas.

3.4.2 Step 2, modelling subsurface pressure head

Step 2 was performed using the Transient Rainfall Infiltration and Grid-Based Regional Slope-Stability Analysis (TRIGRS) program (Baum et al. 2010; Alvioli and Baum 2016), version 2.1. In most applications, TRIGRS computes pressure head and factor of safety distributed over a digital landscape to yield a series of grids representing changes in pressure head and factor of safety through time during a rainfall event. For this work, our objective was a landslide susceptibility map that shows where landslides induced by intense rainfall are most likely, so we used a presumed wettest-case pressure head, rather than simulating time-varying pressure head. This approach greatly accelerated the Step 2 pressure-head computations and eliminated the need to calibrate soil hydraulic parameters. Given the extreme rainfall during Hurricane María and other historical tropical storms, full saturation with the water table at the ground surface and groundwater flow sub-parallel to the ground surface (as determined by the permeability contrast at the soil-saprolite or soil-bedrock boundary) represented the likely wettest-case hydrologic conditions for landslide initiation. This approach neglects effects of suction stress, heterogeneity, and transient pore pressures at the cost of making the susceptibility map more conservative (more false positives). Thus, for this assessment we estimated pressure head for these conditions using the following steady-state formula (Iverson 2000; Baum et al. 2010):

$$\psi(Z) = (Z - d)\left[(\cos\delta)^2 - \frac{I_{ZLT}}{K_s}\right] \tag{1}$$

324   In Eq. (1), $\psi(Z)$ [L] is the pressure head as a function of Z [L], the vertical coordinate direction (positive downward

325   from the ground surface); d [L] is the steady-state depth to the water table measured in the vertical direction (0 m in

326   this case); I_{ZLT} [LT^{-1}] is the steady background flux; δ is the slope angle; and K_s [LT^{-1}] is the saturated hydraulic

327   conductivity. The dimensionless ratio I_{ZLT}/K_s in Eq. (1) accounts for downward percolation and reduces the pressure

328   head from the slope parallel case represented by $H\cos^2\delta$, where H ($=Z-d$) is the column height as noted previously.

329   The average rate of downward percolation is strongly controlled by the permeability contrast between the mobile

330   regolith (soil mantle) and underlying weathered bedrock or saprolite. For the problem considered here, $I_{ZLT}/K_s = 0.028$,

331   consistent with wet initial conditions (averaging 2-25 mm/day of precipitation-induced infiltration, I_{ZLT}, for K_s in the

332   range $10^{-5} – 10^{-6}$ m/s, typical of soils in the study area). This value of I_{ZLT}/K_s directs flow slightly downward and

333   reduces the pressure head by less than 1% compared to slope-parallel flow in the 25° – 55° range of slopes where most

334   landslides occurred. TRIGRS computes $\psi(Z)$ for a series of equally spaced depths between the ground surface ($Z=0$)

335   and a user-specified maximum depth, $Z=Z_{max}$. For this analysis, $Z_{max} = H$ as determined by the soil depth modeled in

336   stage A and we used a depth increment of $Z_{max}/10$.

337   **3.4.3 Step 3, 1D factor of safety**

338   TRIGRS computes the 1D factor of safety, F_1, using the infinite slope analysis (Taylor 1948; Iverson 2000) according

339   to the following formula for the saturated case:

340
$$F_1 = \frac{\tan \phi\prime}{\tan \delta} + \frac{c\prime - \psi(Z)\gamma_w \tan \phi\prime}{Z\gamma_s \sin \delta \cos \delta} \tag{2}$$

341   In Eq. (2) γ_s is the saturated unit weight of soil; γ_w is the unit weight of water; and δ is the true dip of the slip surface

342   at the base of mobile regolith (assumed parallel to the slope of the ground surface in the infinite slope analysis).

343   TRIGRS computes F_1 at the same series of depths between the ground surface and modeled soil depth as for $\psi(Z)$.

344   Eq. (2) is strictly valid for landslides much longer than their depth on planar slopes in which lateral variation in stress

345   is negligible. With the advent of high-resolution topography, the depth-to-length ratios of soil columns at most grid

346   cells have become much greater than 0.1, such that the small depth-to-length landslide assumption of Eq. (2) is

347   violated. This violation reduces accuracy for nonplanar slopes and for rough DEMs (whether the roughness results

348   from natural surface roughness or from data collection and processing errors). A slope-stability analysis that considers

349   multiple adjacent DEM cells can improve accuracy for nonplanar slopes and rough DEMs.

350   **3.4.4 Step 4, 3D factor of safety**

351   To overcome the limitations of F_1 for high-resolution topography and to assess the stability of potential source areas

352   similar in size to past landslides, the computed pressure head, Eq. (2), was used in a separate computer program,

353   Slabs3D (Baum 2023), to compute the quasi-3D factor of safety, F_3. Baum et al. (2012) described and tested a

354   preliminary version of the program, which recently was further developed and tested for the work reported here.

355   Slabs3D was designed to rapidly analyze stability of the soil mantle on hillsides to identify potential shallow landslide

356   sources. By using a method of columns, Slabs3D overcomes some of the limitations of infinite-slope computations on

357   high-resolution topography. However, the current version of Slabs3D relies on force equilibrium alone (not moment

358   equilibrium). Thus, the approximations made in computing F_3 are suitable only for thin (disc- or slab-shaped)

359   landslides, such as most landslides in the study areas (Figs. 2, 3). Potential landslides can be more thoroughly analyzed

360   with 3D slope-stability software such as Scoops3D, which considers moment equilibrium on arcuate trial surfaces

361   (Reid et al. 2015). However, in consideration of the thin, slab-shaped landslide sources and the large area (about 1000

362   km^2) to be analyzed, we deemed the accuracy of Slabs3D sufficient and its speed to outweigh any potential

363   improvements in accuracy offered by Scoops3D. Slabs3D computes F_3 as follows (Hovland, 1977):

364
$$F_3 = \frac{\sum [(H\gamma_s - \psi\gamma_w)\ell_x\ell_y \cos\delta \tan\phi\prime + c\prime A]}{\sum H\gamma_s\ell_x\ell_y \sin\delta_a} \tag{3}$$

365   In Eq. (3), the sums are taken over all the columns within the potential landslide. The quantities ℓ_x and ℓ_y are the

366   horizontal grid cell dimensions; the column height, H, is taken as the modeled soil depth from Step 1; δ_a is the apparent

367   dip of the basal slip surface, $b=b(x, y)$, along the (assumed) direction of sliding. A is the true area of the failure surface

368   at the base of the column (Hovland 1977; Hungr et al. 1989).

369
$$A = \ell_x\ell_y \sqrt{1 + \left(\frac{\partial b}{\partial x}\right)^2 + \left(\frac{\partial b}{\partial y}\right)^2} \tag{4}$$

370   The choice to take H as the modeled soil depth at each grid cell in Eq. (3) is consistent with field observations and

371   previous modelling results. As noted previously, our field observations indicated that the base of most landslide

372   sources occurred directly above a strength and permeability contrast. Except for cases of very rapid infiltration,

373   TRIGRS computes the lowest factor of safety at Z_{max}. Smoothing the modeled soil depth reduces potential irregularities

374   in the trial surface. Tests indicated that modest irregularities have only minor effect on F_3 (Baum, 2023).

375   In Eq. (3), the effect of pore pressure has been computed in a manner consistent with the normal application of the

376   principle of effective stress by subtracting the pore pressure or suction stress from the gravity-induced stress rather

377   than computing the resultants of pore pressure and gravity stress acting normal to the trial failure surface separately

378   as in some implementations of the ordinary method of slices (Turnbull and Hvorslev 1967). Despite its limitations,

379   Hovland's (1977) method of columns is always able to compute a factor of safety and is not subject to the convergence

380   problems that occasionally occur with more sophisticated limit-equilibrium methods.

381   As noted previously in the 1D analysis, Eq. (2) computes F_1 at each grid cell for a range of depths from the ground

382   surface down to a user-specified maximum depth, which in this case is the computed soil depth, H, from step B.1

383   (Baum et al. 2008, 2010). For the cases tested here, the minimum F_1 always occurred at the base of soil, so we limited

384   our search for 3D potential failures to those that follow the base of soil. In computing F_3, we searched the entire digital

385   elevation model (DEM) for potential failures to a maximum depth of H using a circle of fixed diameter (in map view)

386   centered at each grid cell to define the base of potential failure surfaces (one per grid cell, Fig. 7). Average dip direction

387   of the base of soil within the circle determined the assumed slip direction. Potential failure surfaces enclosed by partial

388   circles near the edges of the DEM were excluded from the analysis. Consequently, we extended the DEM grid well

389   beyond the area needed for the final susceptibility map so that any inaccurate F_3 values near the DEM grid boundaries

390   could be discarded as described in the Sect. 3.10, "Removing edge effects." This approach of using map-view-circular

391   trial failure surfaces resulted in potential landslides having the shape of an oblong slab or disc of variable thickness

392   with tapered edges and rounded ends (Fig. 7), such that the trial surface was shaped somewhat like a gold pan. Beyond

393   the limits of the search circle, the slab thins as the potential failure surface slopes from the approximate base of soil

Natural Hazards
and Earth System
Sciences

Discussions

Open Access

EGU

394   toward the ground surface. The failure surface at the head and flanks of the potential slides was assumed (based on

395   Rankine theory, Lambe and Whitman 1969; Terzaghi et al. 1996) to slope $90°-\phi'/2$ and beneath the toe to slope δ_g-

396    $\phi'/2$ (where δ_g is the slope of the ground surface) from the ground surface down to the edge of the circle (Fig. 7). We

397   estimated the contributions of wedges of material at the head, toe, and sides to total driving and resisting force by

398   substituting formulas for height, length, width, average pressure head, and basal area (H, ℓx, ℓy, ψ, and A) of each side

399   wedge, into Eq. (3) (Fig. 7), rather than subdividing the wedges into their component square columns or partial

400   columns and summing their individual contributions. The size of these wedges is negligible with a grid resolution

401   greater than the depth, H, as is often the case for our study areas, with soil depth commonly less than the 1-m resolution

402   of our DEM. The wedge formulas are exact only for constant H. Although variable H across the trial surface introduces

403   minor uncertainty into F_3, the formulas are sufficiently accurate for estimating the value of F_3 for assessing stability

404   of the soil mantle over large areas.
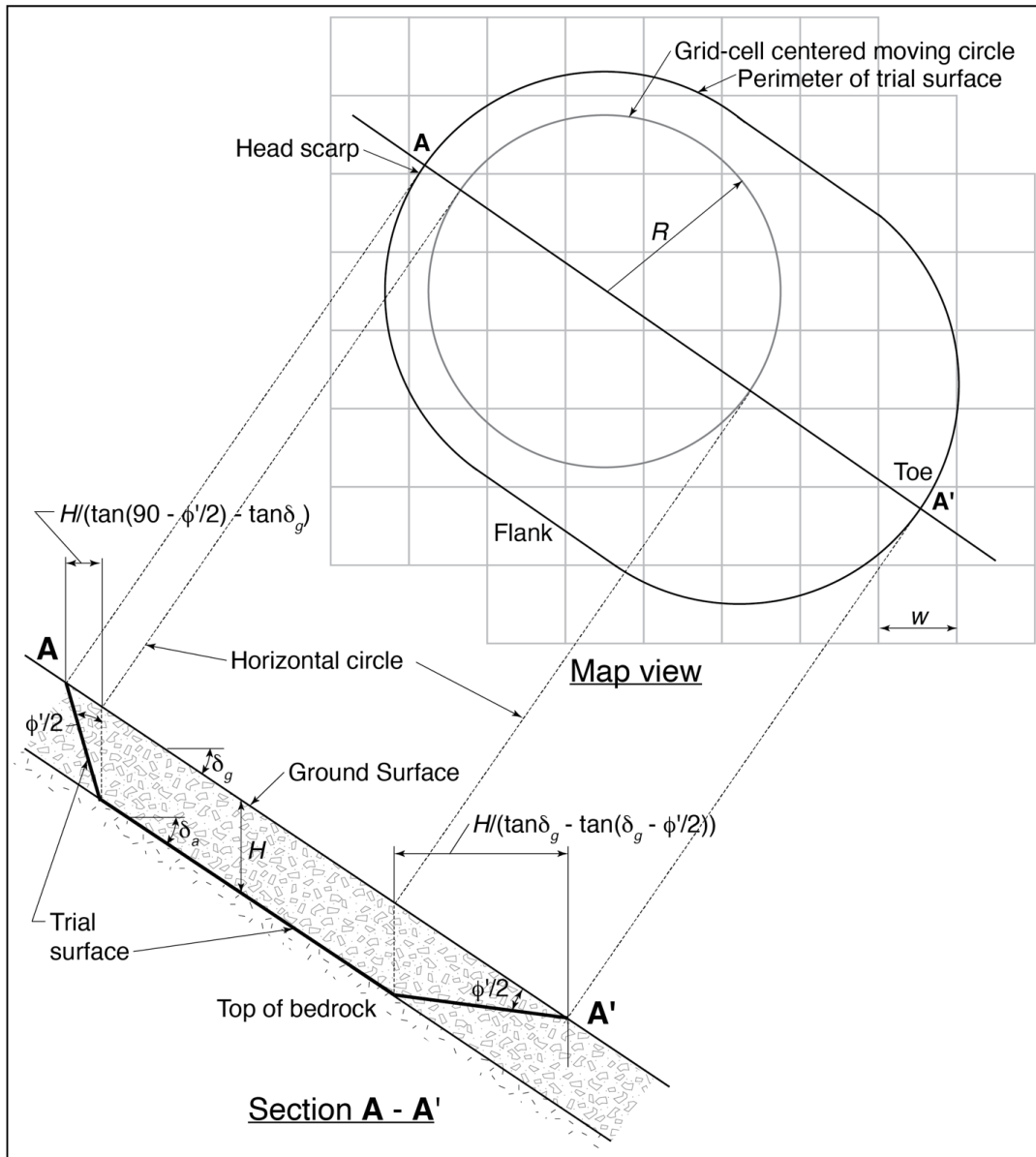
Figure 7. Sketch showing moving circle search strategy and trial surface geometry used in computing approximate 3D factor of safety, F_3. All grid cells whose center is inside the circle are included in the computation of F_3, and cells in the head scarp, flank, and toe areas are combined to form wedges for computational purposes. The trial surface has a map-view radius R; δ_g is the slope of the ground surface; δ_a is the apparent dip of the trial surface in the assumed direction of sliding (average slope direction of grid cells centered within the horizontal circle); H is height of a grid-cell centered column from the trial surface to the ground surface; and ϕ' is the angle of internal friction of the soil for effective stress (modified from Baum et al. 2012). For the case depicted in Section A-A′ (above), H is constant and 1.5 times the horizontal width, w, of the square grid cells. As the average value of H/w decreases and as R increases, the perimeter of the trial surface contracts toward the projection of the horizontal circle onto the ground surface. For variable soil-depth models, H may vary from cell to cell and the value of H for the grid cell closest to the upslope or downslope edge of the horizontal circle is used in the formulas shown in the cross section for horizontal dimensions of the scarp and toe respectively.

417 **3.5 Soil-depth model calibration**

418 Soil-depth model calibration proceeded first by fitting soil models to depth observations followed by checking how

419 the best-fitting models performed as input for computing F_1 to predict landslide locations (see Sect. 3.6). Both

420 calibration and checking made use of pre-event 1-m bare-earth lidar digital elevation models for the four ~2-km^2

421 calibration areas representing the dominant (three) geologic terranes affected by landslides in the study areas (Fig. 1).

422 Landslides had previously been mapped (Bessette-Kirton et al. 2019c) and characterized (Baum et al. 2018) in these

423 four calibration areas (Sec. 2.2, Fig. 3). Tello (2020) described the soil-depth calibration procedures in detail. We

424 summarize important steps here: Field-measured landslide scars on unmodified hillsides (no obvious cut or fill) served

425 as calibration points for soil depth. Tello (2020) adjusted GPS location of each calibration point to the center of its

426 corresponding landslide polygon mapped from imagery by Bessette-Kirton et al. (2019c). A 5-m buffer around each

427 point ensured adequate sampling of model depths to be compared with the field-measured maximum depth. Tello

428 (2020) used a provisional version of the soil-depth code, REGOLITH (Baum et al. 2021), to model trial soil-depth

429 distributions for the calibration areas. Multiple runs to incrementally sample the parameter spaces of several different

430 soil models implemented in REGOLITH produced hundreds of trial soil depth grids for each of the four calibration

431 areas. Soil models tested include a linear area- and slope-dependent model (LASD) (Ho et al. 2012) and modified

432 forms of Pelletier and Rasmussen's (2009) non-linear slope- (NSD), area- and slope- (NASD), and slope- and depth-

433 dependent (NDSD) models. Testing these against the field-measured landslide-scar maximum depths resulted in

434 optimized input parameters for each model and area (Tello 2020).

435 Tello (2020) used a range of statistical metrics identified by Gupta et al. (2009) to determine predictive success of the

436 model outputs. Most important of these was the Euclidian distance from the ideal point, *ED*. The ideal point is

437 characterized by perfect correlation between observed and simulated points and by perfect agreement between the

438 means and standard deviations of the observed and simulated point distributions,

439 $$ED = \sqrt{(r-1)^2 + (\alpha-1)^2 + (\beta-1)^2}$$ (5)

440 where the ideal point is at r=1, α=1, β=1 so that *ED*=0. The linear correlation coefficient, r, relative variability, α, and

441 the bias relative to the observed sample, β, define the ED in eq. (5) (Gupta et al. 2009). In eq. (5) the relative variability

442 is the ratio of the standard deviation of the simulated values, σ_s, to the standard deviation of the observed values, σ_o,

443 (α=σ_s/σ_o). Likewise, the bias is the ratio of mean of the simulated values, μ_s, to the mean of the observed values, μ_o

444 (β=μ_s/μ_o). The linear correlation coefficient, r, indicates the quality of a least-squares fit of the simulated values to the

445 observed values, with r=1 indicating a perfect fit. The model run having the lowest ED usually had the best fit, unless

446 ED > 1 (Tello 2020). Where ED>1, we chose the model run with β closest to 1 so that the mean simulated depth would

447 be as close as possible to the mean of depth observations (Gupta et al. 2009). The best-fit soil-depth distribution

448 corresponded in turn to a best-fit parameter set for each soil-depth model type. Comparison of best scores for each

449 model type identified the overall best fit of all models tested.

3.6 Soil model evaluation and slope-stability calibration

450

451 To further evaluate the soil-depth modelling results and finish calibrating the slope-stability model, we computed F_1

452 for dry and saturated soil conditions using the better performing soil-depth models for each calibration area. Previously

453 defined better performing (TPR ≥ 75%) ranges of φ′ and c' (Baum 2021; Fig. 5b, 5c, 5d) defined the parameter space

454 for computing F_1 with a well-performing subset of trial soil-depth distributions. In addition, we required $F_1 > 1$ in

455 99.9% of grid cells for $\psi(H)=0$ to ensure slope stability under dry conditions. Computing F_1 over the calibration areas

456 using the best-fit distributions for each soil-depth model type and ϕ′ and c' combinations produced many F_1 grids.

457 Receiver Operator Characteristics (ROC) analysis (Fawcett 2006; Begueria 2006) of these F_1 grids against mapped

458 landslide scarp points indicated which combinations of trial soil-depth distribution and strength parameters predicted

459 the most observed landslides, based on the area under the ROC curve. Using parameters from the highest performing

460 F_1 distribution, we selected the preferred soil depth model and ϕ′ and c' values for modelling F_1 in the large study

461 areas enclosing Lares, Utuado, and Naranjito municipalities. The calibration areas represented different geologic

462 terranes having the highest densities of landslides in the study areas so that the calibration procedure yielded separate

463 model and parameter values relevant to each of these terranes.

464 After H and F_1 values had been improved as much as possible by calibration, we began test calculations of F_3 and

465 worked to further refine potential landslide source areas. We varied the size of the trial surface from a 3.5-m radius to

466 a 10.5-m radius (Fig. 7) and used ROC analysis along with information about observed source-area sizes to determine

467 the optimum F_3 radius. Due to insufficient data, rigorous calibration was not possible for some parameter zones, such

468 as the karst areas of Bawiec's (1998) Limey sediment terrane. We adjusted model parameters (reduced maximum soil

469 depth, H_{max}, and characteristic soil depth, h_0, for the soil-depth model and increased c' for computing F_1 and F_3) for

470 the Limey sediment terrane's parameter zone to account for the terrane's low landslide density during Hurricane María.

3.7 Geologic mapping and parameter zonation

471

472 Bawiec (1998) compiled published 1:20,000-scale geologic mapping of Puerto Rico and (as noted previously)

473 combined related formations into geologic terranes (Fig. 1 and Bawiec 1998). Based on the results of early studies

474 (Bessette-Kirton et al. 2019a) and our calibration efforts, the geologic terranes became the basis for subdividing the

475 study areas into parameter zones. The topographic base maps available at the time of geologic mapping lacked the

476 detail of the pre-event lidar-derived topography used in this study. Trial computations of F_1 and F_3 on the study area

477 DEM tiles indicated that a uniform soil depth model across the highly susceptible geologic terranes resulted in a more

478 accurate susceptibility map than a zoned model using the calibrated soil depth parameters. Uniform values of ϕ′ and

479 c' for the highly susceptible geologic terranes likewise resulted in good performance so we used the same soil depth

480 and strength parameters for all three terranes (Supplemental Figures S1 and S2). Consequently, slight uncertainty in

481 locations of boundaries between these terranes had no effect on computed F_1 and F_3 values. However, a large

482 difference in landslide susceptibility and model parameters (maximum soil depth, h_0, c') existed between the Limey

483 sediment terrane with its cone karst and the highly susceptible terranes of the basement complex (submarine basalt,

484 volcaniclastic, and granitoid). Offsets as great as tens of meters in the contact between the Limey sediment terrane

485 and its neighbors along a prominent escarpment in Lares and Utuado resulted in errors in F_1 and F_3 along the

486   escarpment. Consequently, Perkins et al. (2022) remapped the Limey sediment contact using lidar-derived shaded

487   relief images and optical imagery to accurately delineate the transition from high to low landslide susceptibility across

488   the contact. The contact was discerned based on the visually distinct differences between the closed basins and rugged

489   karst cones of the Limey sediment terrane and the steep ridges and narrow branching valleys of the basement rocks.

3.8 Soil-depth modelling

491   After completing the calibration process, we created the overlapping rectangular tiles (described previously, Sec. 1.0,

492   3.1) from the pre-event lidar bare-earth DEMs (Fig. 6, stage B and Fig. 1b, 1c). We created additional input files from

493   the lidar-derived DEM tiles: flow accumulation grids for use with the area-dependent soil-depth models and

494   parameter-zone grids for specifying different model input parameters (Sec. 3.6, 3.7 and step B.1, Fig. 6). The

495   parameter zones ensured a thinner and less continuous modeled soil mantle in the karst (Limey sediment terrane) than

496   in areas underlain by the landslide-prone geologic terranes (Fig. 1).

3.9 Pressure-head and slope-stability modelling

498   Raster grids created from the soil-depth modelling defined soil depth (H) and slope of the ground surface at each grid

499   cell in TRIGRS. We computed ψ and F_1 using TRIGRS as described previously using the same lidar-derived DEM

500   tiles and parameter zones as for soil-depth modelling (steps B.2 and B.3, Fig. 6). Then, using $\psi(H)$ computed with

501   TRIGRS along with the same lidar tiles, parameter zones, and ϕ' and c' values used in computing F_1 as input for

502   Slabs3D, we computed F_3 (step B.4, Fig. 6). The radius of each trial surface, as constrained by earlier testing in the

503   calibration areas (Sect. 3.6, 4.5), was held constant at 3.5 m for all model runs on study area tiles.

504   After modelling potential source areas on pre-event topography, we recomputed the models using post-event 1-m lidar

505   topography (U.S. Geological Survey, 2020a, b, c). We generated new slope, zone, and flow-accumulation grids from

506   the post-event lidar and then ran REGOLITH, TRIGRS, and Slabs3D in succession (Fig. 6, steps C.1, C.2, C.3, and

507   C.4) to indicate our best estimate of susceptibility to future landslide initiation.

3.10 Removing edge effects

509   To reduce edge effects (Fig. 6, step C.5) when joining the four overlapping tiles for Lares and Utuado to create a final

510   map (based on post-event lidar), we first removed a 100-m buffer along all edges of each tile. At grid cells where two

511   tiles overlapped, differences in F_3 tended to be small and we retained the greater F_3 value. For the single tile covering

512   Naranjito, we removed only the 100-m buffer along all tile edges.

3.11 Model testing and evaluation

514   We used ROC analysis of F_3 grids based on pre-event lidar topographic data compared to landslide head-scarp points

515   mapped by Hughes et al. (2019) as a basis for testing performance and then defining susceptibility categories (step

516   B.5, Fig. 6). Selecting the minimum F_3 value within a 3-m radius around the scarp points accounted for uncertainty in

517   their mapped locations. Validating F_3 for pre-event topography was appropriate because it most accurately portrayed

518   conditions at the time of Hurricane María. We computed true positive rate (TPR), false positive rate (FPR), and area

519   under the TPR-FPR curve (AUC) and distance from the ideal point (d_{IP}), (0,1), to evaluate performance of pre-event

520   F_3 as a predictor of observed landslide scarp points. Analyzing landslide density distribution across F_3 provided a

521   further check on model accuracy. We computed landslide densities in 0.1 increments of F_3 to check for a general trend

522   of decreasing observed density with increasing F_3. In addition to these quantitative assessments, we inspected the

523   maps to confirm that the susceptibility zones and potential source areas made sense topographically, mechanically,

524   and geologically. These inspections helped ensure that potential landslide source areas were consistent with

525   observations and expectations for hillsides whether they were relatively undisturbed or modified by roads, cut slopes,

526   and embankments. The inspections led to some minor revisions of the computer code to correct errors, followed by

527   repeated model runs.

528

529   As an additional check we computed ROC statistics for minimum F_3 values within source areas mapped by Baxstrom

530   et al. (2021a) and Einbund et al. (2021a, 2021b). Their detailed landslide source mapping covers only a fraction of the

531   study areas (Fig. 1), whereas the scarp points mapped by Hughes et al. (2019) cover the entire island. However, source

532   area polygons enclose pixels that are more relevant to testing performance of F_3 than circles centered at the scarp

533   points.

534   Evaluating the model to address the need for a conservative landslide susceptibility map led us to select threshold

535   values of F_3 enclosing specific percentages (or TPR) of landslide points. Every F_3 contour on the map encloses a

536   specific percentage of landslide points. Contours at high F_3 values enclose more landslide points than low F_3 contours.

537   We selected F_3 contours corresponding to TPR of 0.75 and 0.90 of Hurricane María-produced landslide head-scarp

538   points (Hughes et al. 2019) to define the limits of very high (TPR ≤ 0.75), high (0.75 ≤ TPR ≤ 0.90), and moderate

539   (TPR > 0.90) landslide source susceptibility zones. These classes include most mapped landslide points as well as the

540   adjacent steep slopes where they occurred, while limiting the overall areal extent of the very high and high

541   susceptibility classes. Using the same F_3 thresholds at TPR ≤ 0.75 and TPR ≤ 0.90 determined for the pre-event

542   topography (step B.5, Fig. 6), we then defined landslide susceptibility zones using post-event topography across the

543   three municipalities (step C.5, Fig. 6). These zones estimate the potential for future shallow landslides.
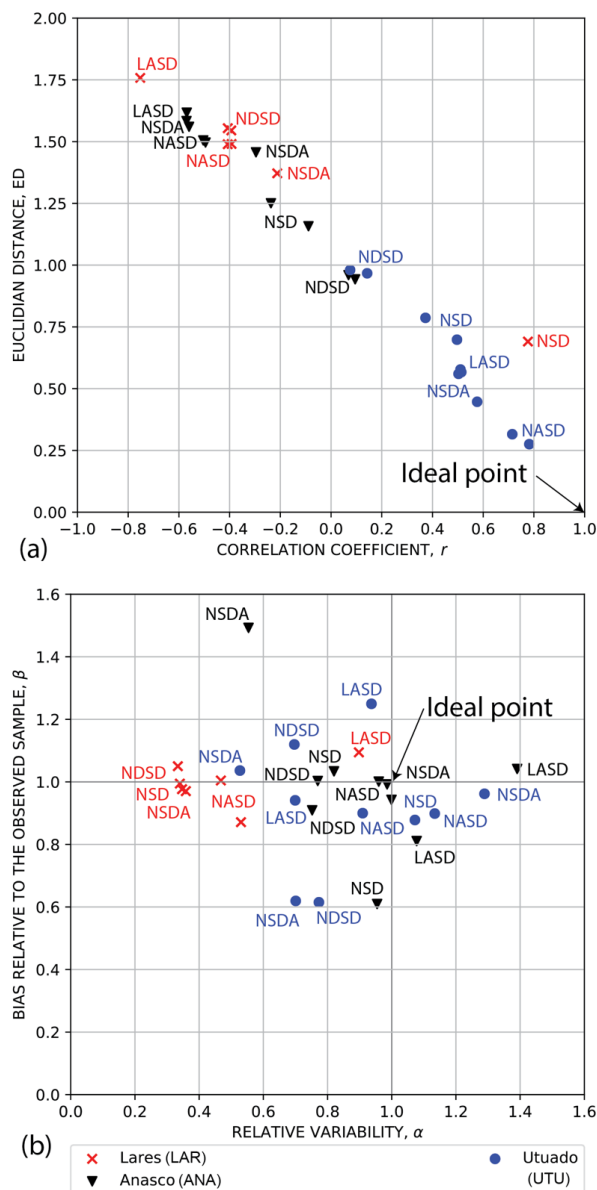

544   **4 Results**

545   **4.1 Soil-depth calibration**

546   We calibrated soil depth to field measurements (Fig. 6, step A.1) for three (ANA, LAR, UTU) of the four calibration

547   areas and calculated Euclidian distance from the ideal point, ED (Eq. 5), correlation coefficient, r (and other statistical

548   parameters as outlined in Tello 2020) to determine which models and parameter sets gave the closest match to field

549   observations (Fig. 8a, b). No soil depth calibration was performed for NAR as depth measurements in Naranjito were

550   mainly outside the area mapped by Bessette-Kirton et al. (2019c). Limiting the observed depths to landslide scars on

551   relatively unmodified slopes resulted in sample sizes of only seven or eight observation points (landslide sources) per

552   calibration area. Most soil-depth models for the Utuado calibration area (UTU) had acceptable performance as

553   indicated by positive correlation between observed and simulated depths (0.08 ≤ r ≤ 0.78), and ED ranging from 0.28

554 to 0.99 (Fig. 8a; Tello 2020). Of these, the modified nonlinear area and slope (NASD) model had the smallest ED,

555 0.28, and the largest r, 0.78 (Fig. 8a). Other better-performing models were a nonlinear slope-dependent model with

556 linear area dependance (NSDA) and a linear area- and slope-dependent model (LASD) based on the wetness index

557 (Ho et al. 2012). In contrast, most soil-depth models for the Añasco (ANA) and Lares (LAR) calibration areas

558 performed poorly, with negative or small positive correlation ($r < 0.16$) and $0.69 < ED < 1.8$ (Fig. 8a). At LAR, only

559 the nonlinear slope dependent model (NSD, see Pelletier and Rasmussen 2009) had acceptable performance with r =

560 0.78 and ED=0.69 (Fig. 8a). The NASD model had α and β closest to 1, for both ANA and LAR (Fig. 8b).

Natural Hazards
and Earth System
Sciences
Discussions

Open Access

EGU

Figure 8. Soil-depth model calibration measures for Anasco (ANA), Lares (LAR) and Utuado (UTU) calibration areas (Fig. 1). Performance is based on comparing maximum landslide depth at field-mapped landslide points against modeled depths within a 5-m radius of the point. GPS point locations were corrected as needed by moving them to the centers of corresponding landslide polygons mapped by Bessette-Kirton et al. (2019c). (a) Primary metrics, Euclidian distance from the ideal point, ED (smaller is better), versus correlation coefficient, r, (b) bias relative to the observed sample, β, versus relative variability, α. The ideal point is at $r=1$, $\alpha=1$, $\beta=1$. [Soil-depth models: LASD, linear area- and slope-dependent model; NASD, nonlinear area- and slope-dependent model; NDSD, nonlinear depth- and slope-dependent model; NSD, nonlinear slope-dependent model; NSDA, nonlinear slope-dependent model with linear area dependence].

Natural Hazards
and Earth System
Sciences
Discussions

4.2 Soil model evaluation and slope-stability calibration results

Slope stability calibration compared F_1 values for previously determined ranges of c' and ϕ' (Fig. 5) for each of the soil depth models to find the best-performing combination of soil model and strength parameters for predicting landslide source locations in each calibration area (Fig. 6, steps A.3.aand A.3.b). For UTU, the NASD model performed best with the NSDA model close behind (Tello 2020) based on area under the TPR – FPR curve and distance of the curve from the ideal point. Parameter combinations and ROC results for the best-performing model in each area appear in Table 1. Despite poor soil depth model performance metrics for ANA and LAR (Fig. 8), the F_1 calculations for the three calibration areas indicated that the NASD soil depth model had the greatest predictive strength for locations of landslide source areas in ANA, LAR, and UTU with similar results (Table 1). Despite lack of soil-depth calibration in NAR, results in this study area were like the other three calibration areas (Table 1). Values of δ_c near 60° gave the best soil-depth model results (Table 1), despite variability in the steepest slopes where landslides occurred in the different terranes (Fig. 3d, 4).

Table 1. Calibration results for 1D factor of safety, F_1, with soil depth models by calibration area (Fig. 1). Positives and negatives in the ROC analysis based on total pixels within and outside the estimated source areas of landslide polygons mapped by Bessette-Kirton et al. (2019c) and whether the pixels have $F_1>1$ or $F_1<1$ (Tello 2020). [Symbols and abbreviations: NASD, non-linear area and slope dependent soil-depth model of Pelletier and Rasmussen (2009) as modified by Baum et al. (2021); H_{max}, maximum soil depth; δ_c, critical slope angle; R_d, diffusivity ratio; c', soil cohesion for effective stress; ϕ', angle of internal friction for effective stress; AUC, area under the curve of true-positive-rate (TPR) and false positive rate (FPR) (larger is better); d_{IP}, distance from the ideal point, (0,1), to nearest point on the TPR-FPR curve (smaller is better); Best F_1, 1D factor of safety at point on the TPR-FPR curve nearest to the ideal point, (0,1), and therefore the most accurate F_1 classifier of landslide versus non-landslide grid cells for the particular model (closer to one is better); °, degrees.]

Calibration area	Soil Model	H_{max} (m)	δ_c (°)	R_d	c' (kPa)	ϕ' (°)	AUC	d_{IP}	Best F_1
Utuado (UTU)	NASD	2.0	60	1.0	2.5	45°	0.67	0.48	1.5
Añasco (ANA)	NASD	3.0	60	0.16	4.5	45°	0.70	0.46	1.1
Lares (LAR)	NASD	3.0	60	0.25	4.5	45°	0.66	0.52	1.1
Naranjito (NAR)	NASD	3.0	60	0.2	4.0	45°	0.65	0.54	1.2

4.3 Modeled soil depth

Having completed the soil-depth model calibration (Sec. 4.1) and testing (Sec. 4.2), we modeled soil depth in the larger map tiles preparatory to analyzing slope stability (Fig. 6, step B.1). Each tile covers hundreds of km², so we illustrate results using the NAR area, chosen to demonstrate that our susceptibility workflow can achieve very good results even with limited landslide source depths observations. As noted previously, insufficient field-measured landslide points prevented soil-depth model calibration (Sec. 4.1), but not model evaluation and slope stability

600 calibration (Sec. 4.2) for NAR. Figure 9 shows predicted soil depth for the best performing soil-depth model (based

601 on the slope-stability evaluations, Sec. 4.2) in NAR (see Fig. 1 for location). The model shown in Fig. 9 predicts

602 greater soil depth in hollows than on ridges. Other models that were tested (not shown) produced somewhat similar

603 results. Differences in model structure produce different responses to topographic features, including flat areas, road

604 cuts, and steep slopes. For example, the modified NASD and NSDA models predicted deep soils (≤3 m for parameters

605 chosen) in convergent areas, on steep slopes, including road cuts and embankments; thin soils on ridge crests, and thin

606 or no soil on downslope flat areas (see large flat area on east edge of Fig. 9). In contrast, the LASD and NDSD models

607 predicted deep soils (≤3 m for parameters chosen) in convergent areas and on flats and thin soils on ridge crests and

608 steep slopes (except where they occur in strongly convergent topography). Features were more distinct in the three

609 nonlinear models, NASD, NSDA, and NDSD, than in the linear LASD model.
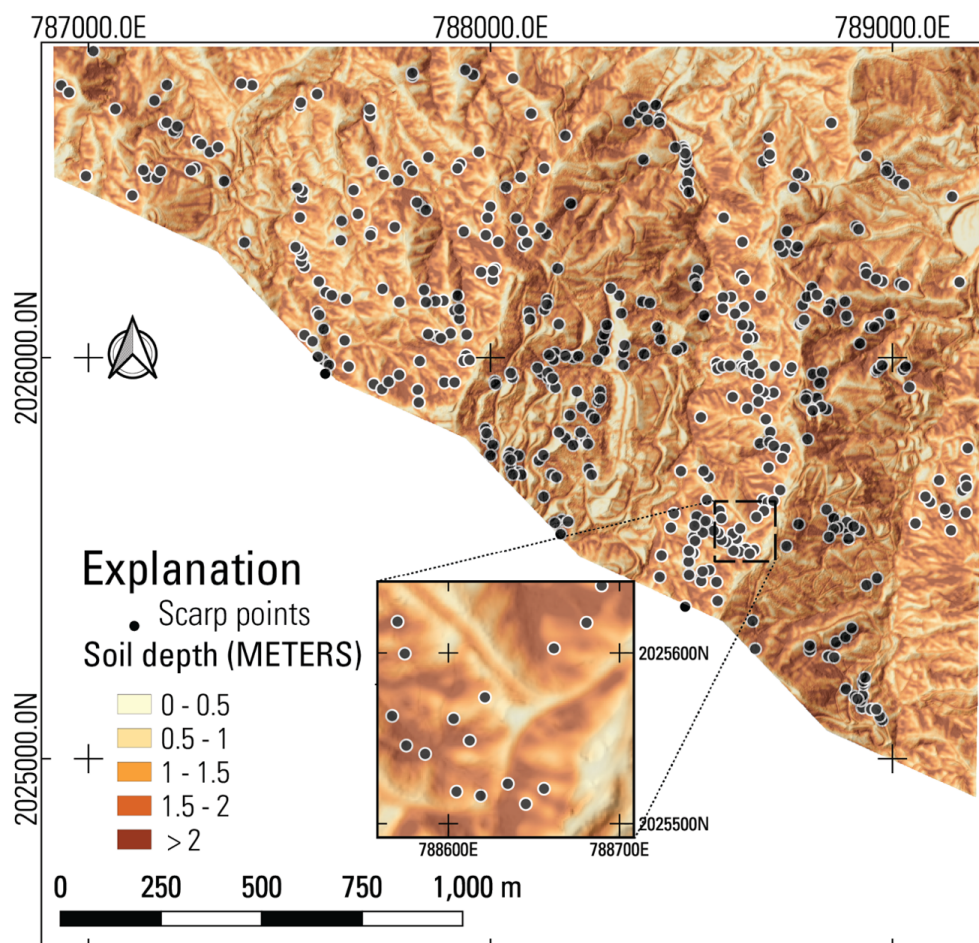
610

611 **Figure 9. Best-performing version of soil depth maps from soil-depth models tested for the Naranjito (NAR) calibration**
612 **area in volcaniclastic terrane (Fig. 1). Topographic base derived from lidar by U.S. Geological Survey (2018), scarp points**
613 **from Bessette-Kirton et al. (2019c). The modified Nonlinear Area- and Slope-dependent (NASD) model (modified from**
614 **Pelletier and Rasmussen 2009, as implemented by Baum et al. 2021) depicted here, was the overall best-fitting soil-depth**
615 **model for this terrane. Inset shows details of a 150 m by 150 m area, with thicker soil accumulation in concave areas.**

4.4 One-dimensional factor of safety

616

617 Figure 10 shows F_1 optimized for NAR and calculated using TRIGRS and the soil model results in Fig. 9, as well as

618 F_1 for constant soil depth. Slopes steeper than 60°, the estimated critical slope angle, were treated as barren and stable

619 because landslides were very rare on slopes steeper than 60° (Fig. 3d). Soil strength parameters are within the ranges

620 obtained by sensitivity analysis of F_1 parameters ϕ' and c' over observed ranges of slope and depth of landslides

621 characterized in the field at ANA, LAR, UTU, and NAR (Fig. 5). The only landslide source locations available

622 throughout the three municipalities are the scarp points of Hughes et al. (2019). Due to location uncertainty, we used

623 a 3-m radius around the scarp points for defining true positives. Color thresholds on the maps (Fig. 10) are based on

624 F_1 at TPR of 0.75, 0.90, and 0.95. Consequently, thresholds for F_1 differ for each panel in Fig. 10. The same TPR

625 values (0.75, 0.90, 0.95) were used for picking F_3 thresholds for landslide initiation susceptibility across the entire

626 study area covering Naranjito, Utuado, and Lares Municipalities in the final maps (Supplemental Figures S1 and S2).

627
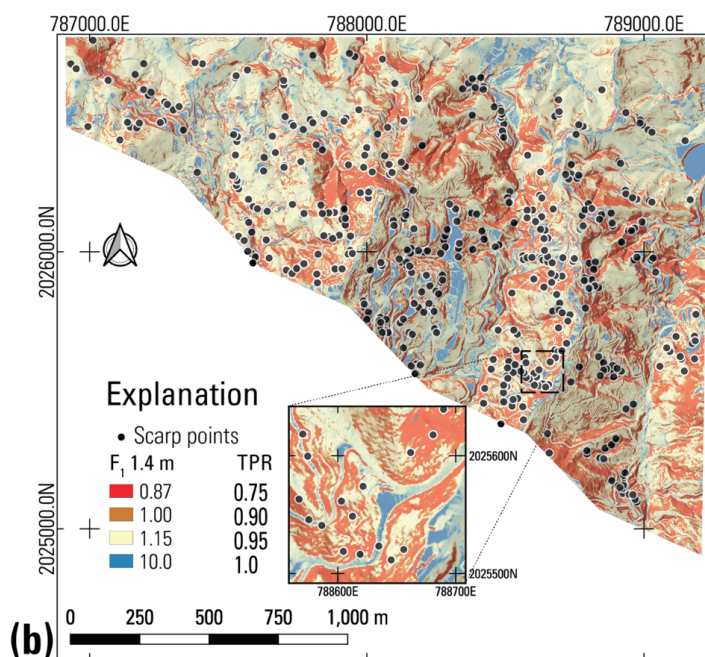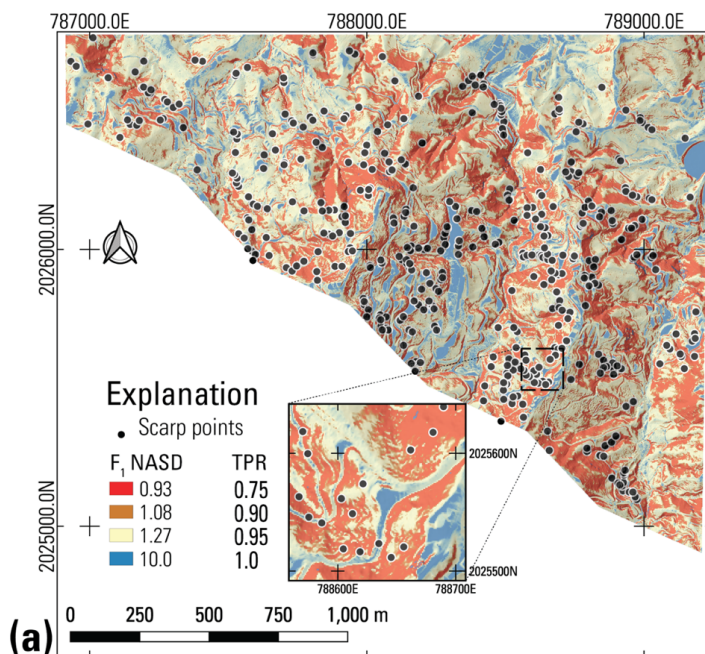
Figure 10. Maps of Naranjito (NAR) calibration area in volcaniclastic terrane (Fig. 1) showing 1D factor of safety (F_1) results for a) soil-depth model shown in Figure 9 as well as b) constant average soil depth. Topographic base derived from lidar by U.S. Geological Survey (2018), scarp points from Bessette-Kirton et al. (2019c). True positives determined by minimum F_1 within a 3-m radius of the scarp points. (a) F_1 for NASD, the modified nonlinear area- and slope-dependent soil-depth model depicted in Fig. 9, (b) F_1 for constant soil depth of 1.4 m. Inset shows details of a 150 m by 150 m area.

633 Areas of low F_1 are similar in overall pattern between the two maps shown in Fig. 10 but differ in detail. These details

634 include small areas of low F_1 unique to each model as well as variation in the extent of major areas of low F_1. Many

635 boundaries of the areas of low F_1 are ragged and small patches of yellow, indicating higher F_1, occur within the larger

636 red and orange areas of low F_1. Differences in F_1 between the maps are attributable mainly to variation in soil depth

637 and partly to variation in c'. The optimum value of c' varied depending on the characteristics of each soil model (Table

638 2). The results shown in Fig. 10 are for the best-performing combination of c' and ϕ' for the soil-depth model at NAR

639 (Fig. 9 and Sec. 4.2) and for constant average depth of 1.4 m.

640 The different F_1 patterns shown in Fig. 10 correspond to slightly different levels of predictive success. The AUC and

641 distance from the ideal point (0,1) to the nearest point on the TPR-FPR curve, d_{IP} indicate that F_1 for constant depth

642 has the highest predictive skill (AUC=0.88, d_{IP}=0.26, F_1 value nearest the ideal point, F_1=0.9). Next, F_1 for the NASD

643 model performed almost as well (AUC=0.86, d_{IP}=0.30, F_1 value nearest the ideal point, F_1=1.0). When applied to the

644 entire DEM tile covering Naranjito municipality, F_1 for constant depth and NASD tied with AUC = 0.86 and d_{IP} =

645 0.30 (constant depth) and d_{IP} = 0.29 (NASD). Thus, the performance edge of constant depth is localized at NAR and

646 does not extend across the entire Naranjito DEM tile. Other soil-depth models performed slightly worse (Table 2)

647 consistent with results obtained by Tello (2020) for UTU. The slightly higher performance for F_1 with constant depth

648 at NAR comes at the cost of the area classified as very high, high, or moderate susceptibility (TPR = 0.95) being more

649 diffuse, with more ragged boundaries, than for F_1 with NASD (Fig. 10a, b). Varying the amount of cohesion used with

650 a particular soil model caused small changes in the AUC, d_{IP}, and best F_1 as shown by the two entries for NDSD in

651 Table 2.

652 **Table 2. Key inputs and performance measures for factor of safety calculations based on the infinite slope model (F_1), as**
653 **implemented by TRIGRS, in the Naranjito calibration area (NAR). Performance is based on minimum F_1 within a 3-m**
654 **radius of landslide scarp points mapped by Hughes et al. (2019). [Symbols and abbreviations: NASD, non-linear area and**
655 **slope dependent soil-depth model of Pelletier and Rasmussen (2009) as modified by Baum et al. (2021); NSDA, non-linear**
656 **slope dependent model of Pelletier and Rasmussen (2009) modified by Baum et al. (2021) to include linear area dependence;**
657 **NDSD, non-linear slope and depth dependent model of Pelletier and Rasmussen (2009); LASD, linear area and slope**
658 **dependent model of Ho et al. (2012); H_{max}, maximum soil depth; δ_c, critical slope angle; R_d, diffusivity ratio; C_0, empirical**
659 **constant used in LASD; c', soil cohesion for effective stress; ϕ', angle of internal friction for effective stress; AUC, area**
660 **under the curve of true-positive-rate (TPR) and false positive rate (FPR) (higher is better); d_{IP}, distance from the ideal**
661 **point, (0,1), to nearest point on the TPR-FPR curve (smaller is better); Best F_1, 1D factor of safety at point nearest to the**
662 **ideal point, (0,1), and therefore the most accurate F_1 classifier of landslide versus non-landslide grid cells for the particular**
663 **model (closer to 1.0 is better); °, degrees ; -- not applicable.]**

Soil Model	H_{max} (m)	δ_c (°)	R_d or C_0	c' (kPa)	ϕ' (°)	AUC	d_{IP}	Best F_1	TPR at d_{IP}
NASD	3.0	60	0.20	4.0	45°	0.86	0.30	1.0	0.82
LASD	3.0	60	0.45	3.5	45°	0.85	0.31	1.1	0.84
NDSD	3.0	60	0.10	4.5	45°	0.82	0.36	1.2	0.75
NDSD	3.0	60	0.10	2.5	45°	0.86	0.32	1.0	0.89
NSDA	3.0	60	0.10	4.5	45°	0.85	0.30	1.1	0.80
Constant	1.4	60	--	4.0	45°	0.88	0.26	0.9	0.79

664

Natural Hazards
and Earth System
Sciences
Discussions
Open Access
EGU

4.5 Quasi-three-dimensional factor of safety

Figure 11 shows F_3 computed using the soil-depth model in Fig. 9 and constant soil depth of 1.4 m. Predictive skill for F_3 is somewhat less than F_1; AUC is 0.05 – 0.08 less for F_3 than corresponding F_1 (Tables 2 and 3). The only exception is for the constant soil depth model results where F_3 has the highest AUC, 0.94, of all cases tested (Fig. 12a and 12b). Despite the overall slightly worse performance of F_3 it provided smoother boundaries on the landslide susceptible areas (Fig. 11a, b), which also are more continuous than corresponding F_1 landslide susceptible areas (Fig. 10). The lower AUC values resulted from the F_3 susceptible areas covering slightly more land area than the corresponding F_1 areas at the same TPR. Therefore, the F_3 susceptibility maps are more conservative than their F_1 counterparts.
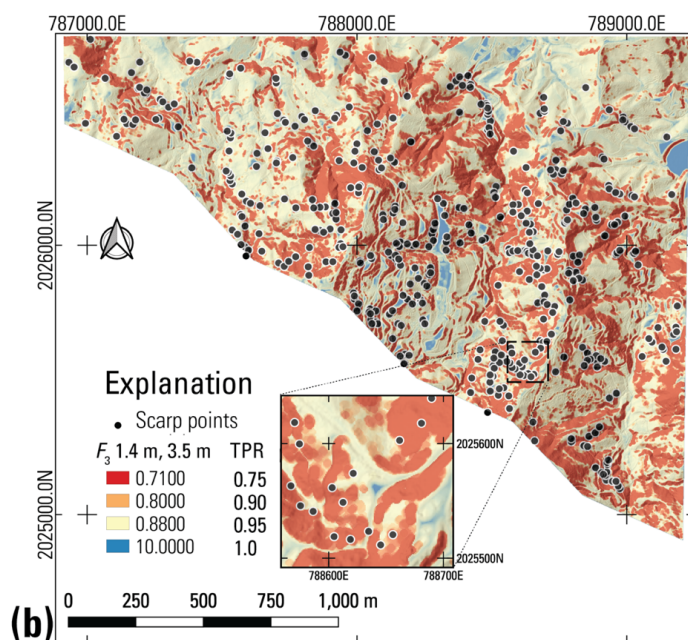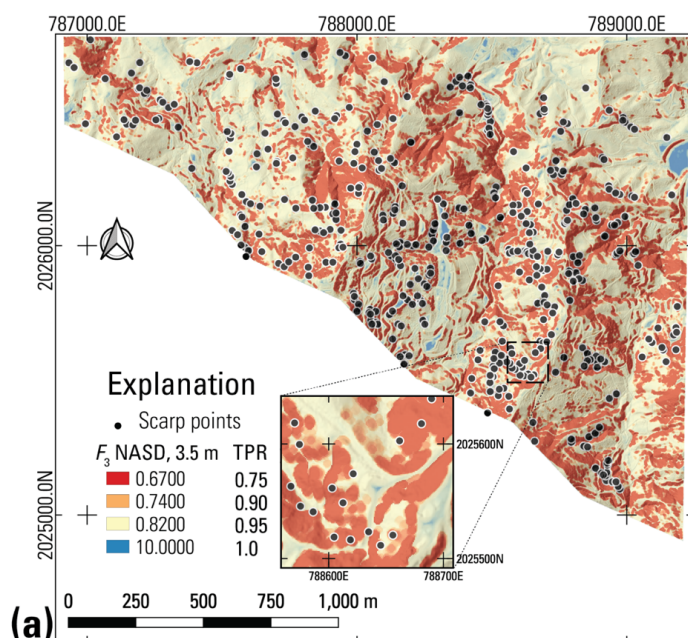
Table 3. Key inputs and performance measures for factor of safety calculations based on a quasi-3D limit-equilibrium slope stability model (F_3) in the Naranjito calibration area (NAR). Performance is based on minimum F_3 within a 3-m radius of landslide scarp points mapped by Hughes et al. (2019). [Symbols and abbreviations: NASD, non-linear area and slope dependent soil-depth model of Pelletier and Rasmussen (2009) as modified by Baum et al. (2021); NSDA, non-linear slope dependent model of Pelletier and Rasmussen (2009) modified by Baum et al. (2021) to include linear area dependence; NDSD, non-linear slope and depth dependent model of Pelletier and Rasmussen (2009); LASD, linear area and slope dependent model of Ho et al. (2012); H_{max}, maximum soil depth; δ_c, critical slope angle; R_d, diffusivity ratio; C_0, empirical constant used in LASD; c', soil cohesion for effective stress; ϕ', angle of internal friction for effective stress; AUC, area under the curve of true-positive-rate (TPR) and false positive rate (FPR); d_{IP}, distance from the ideal point, (0,1), to nearest point on the TPR-FPR curve; Best F_3, 3D factor of safety at point nearest to the ideal point, (0,1), and therefore the most accurate F_1 classifier of landslide versus non-landslide grid cells for the particular model (closer to 1.0 is better); °, degrees.]

Soil Model	H_{max} (m)	δ_c (°)	R_d or C_0	c' (kPa)	ϕ' (°)	Trial surface radius (m)	AUC	d_{IP}	Best F_3	TPR at d_{IP}
NASD	3.0	60	0.20	0.5	45°	3.5	0.80	0.38	0.9	0.86
NASD	3.0	60	0.20	0.5	45°	6.5	0.75	0.45	0.9	0.66
NASD	3.0	60	0.20	0.5	45°	9.5	0.71	0.50	1.0	0.86
LASD	3.0	60	0.45	0.5	45°	3.5	0.78	0.44	1.0	0.89
NDSD	3.0	60	0.10	0.5	45°	3.5	0.78	0.40	0.9	0.71
NSDA	3.0	60	0.10	0.5	45°	3.5	0.80	0.37	0.9	0.78
Constant	1.4	60	--	0.5	45°	3.5	0.92	0.23	1.0	0.94

Tests indicated that trial surfaces having a map-view radius of 3.5 m provided more accurate estimates of susceptible areas than larger trial surfaces (6.5-m and 9.5-m radius). Other things being equal, larger trial surfaces resulted in smaller AUC and larger d_{IP} (Table 3, Fig. 12b). The larger trial surfaces tended to widen the susceptible areas and smooth their boundaries, with the result that a larger percentage of the calibration area was classified as susceptible (9.5-m radius, 85%; 6.5-m radius, 83%; 3-m radius, 78% for examples in Table 3). In addition, the 3.5-m radius produced a trial surface close in size (7.5 – 7.9 m wide, with an area of 46 – 48 m^2 at the ground surface for 1-m depth on 30° – 40° slopes) to the median horizontal areas of landslide sources mapped in NAR, 51 m^2, in UTU2, 42 m^2, and in LAR2 64 m^2 (Fig. 3c).

Natural Hazards
and Earth System
Sciences
Discussions
Open Access
EGU

694

695

696 **Figure 11. Maps of Naranjito (NAR) calibration area in volcaniclastic terrane (Fig. 1) showing quasi-3D factor of safety,**
697 **F_3, results for the soil depth models shown in Figure 9. (a) F_3 for the modified nonlinear area and slope dependent (NASD)**
698 **soil-depth model depicted in Fig. 9, (b) F_3 for constant soil depth of 1.4 m. Inset shows details of a 150 m by 150 m area. The**
699 **calculation of F_3 used a trial surface of 3.5-m map-view radius (Fig. 7). Topographic base derived from lidar by U.S.**
700 **Geological Survey (2018), scarp points from Bessette-Kirton et al. (2019c).**

701
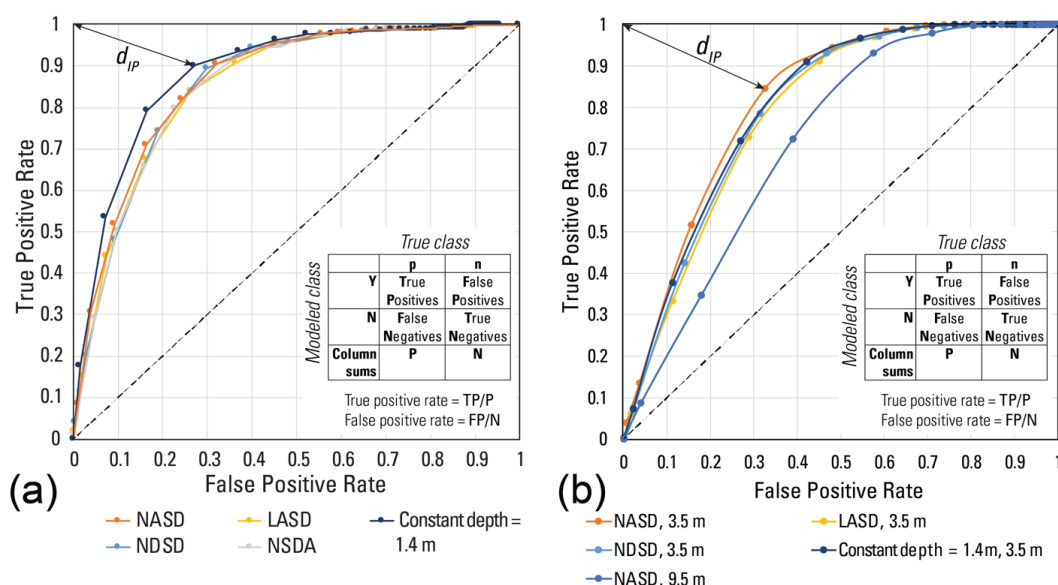
702

703 **Figure 12. Graphs of true positive rate (TPR) versus false positive rate (FPR) for factor of safety maps in Naranjito**
704 **calibration area (NAR in Fig. 1a, 1c). Inset shows confusion matrix and formulas defining true positive rate and false**
705 **positive rate. Double-headed arrow indicates distance from ideal point (d_{IP}) for the results of the factor of safety with the**
706 **smallest d_{IP}. (a) TPR-FPR results for 1D factor of safety (F_1) in Fig. 10, as well as results for F_1 using other soil-depth models**
707 **that were tested during the calibration process. (b) TPR-FPR results for quasi-3D factor of safety (F_3) in Fig. 11, as well as**
708 **results for F_3 using other soil depth models and one with a larger (NASD, 9.5-m radius) trial surface. [Soil-depth models:**
709 **LASD, linear area- and slope-dependent model (Ho et al. 2012); NASD, modified nonlinear area- and slope-dependent**
710 **model (modified from Pelletier and Rasmussen 2009); NDSD, nonlinear depth- and slope-dependent model (Pelletier and**
711 **Rasmussen 2009); NSD, nonlinear slope-dependent model (Pelletier and Rasmussen 2009); NSDA, nonlinear slope-**
712 **dependent model with linear area dependence (modified by Baum et al. 2021 from NSD model of Pelletier and Rasmussen**
713 **2009)].**

714 **4.6 Susceptibility categories and predictive strength**

715 Computing F_3 over the combined study areas of Lares, Utuado, and Naranjito municipalities produced somewhat

716 different results than in the calibration areas. Calibration areas have very high landslide densities, with average density

717 of 182 scarps/km^2 at NAR. However, landslide density varies considerably across each municipality. Based on positive

718 correlation between low F_3 and landslide scarp points mapped by Hughes et al. (2019), we established susceptibility

719 categories based on percentages of landslides enclosed by successive susceptibility categories as noted previously and

720 as shown in Table 4. Increasing density of observed landslides is consistent with increasing susceptibility. Very high

721 susceptibility (typically > 118 scarp points/km^2) characterizes 23% of the total study area and 21%, 43%, and 45% of

722 the area underlain by marine volcaniclastic, submarine basalt, and granitoid rocks, respectively. Almost all karst areas

723 underlain by limey sediments had low susceptibility (< 2 scarp points/km^2) (Baxstrom et al. 2021b). Based on the

724 information in Table 4, the AUC for the entire map area is 0.84, and d_{IP} is 0.34.

725 Due to physical (subsurface conditions, ground-failure mechanisms) and conceptual (parameters, models)

726 uncertainties, the F_3 value at the boundary between high and moderate susceptibility is slightly less than 1 (0.97, Table
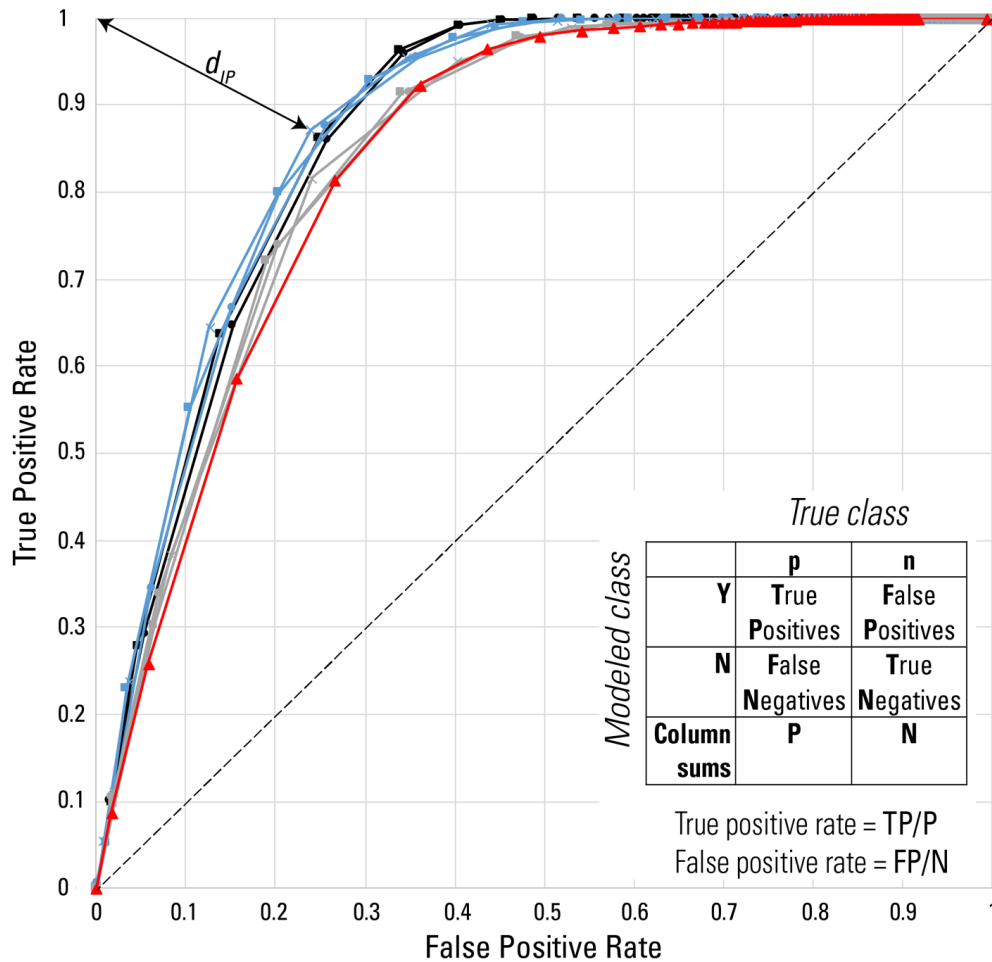
727   4). Although the strength parameters could be increased to achieve $F_3 = 1.0$ at TPR = 0.90, we also wanted to keep F3

728   at TPR = 0.95 relatively low while keeping $F_3 > 1$ under dry conditions for as much area as possible. Our final model

729   parameters represent a compromise between stable slopes ($F_3 > 1$) under dry conditions and low factor of safety (F_3

730   < 1) for highly susceptible slopes under presumed wettest conditions.

731   Recent, detailed mapping of source areas provided an opportunity to further test performance of the pre-Hurricane

732   María F_3 map (output from step B.5, Fig. 6). Figure 13 shows TPR-FPR curves for the pre-Hurricane María F_3 map

733   tested against Hurricane María landslide source polygons (Baxstrom et al. 2021a; Einbund et al. 2021a, 2021b) and

734   against scarp points (Table 4). The AUC range, 0.85 – 0.88, is somewhat greater than obtained by testing within a 3-

735   m radius of the scarp points, 0.84.

736

737   **Table 4. Landslide susceptibility categories based on minimum value of quasi-3D factor of safety, F_3, within a 3-m radius**
738   **of landslide scarp points mapped by Hughes et al. (2019) for all three municipalities. For consistency, F_3 thresholds below**
739   **are based on F_3 calculated using pre-Hurricane María lidar topography and scarp locations of landslides induced by**
740   **Hurricane María.**

Landslide Susceptibility	F_3 threshold	Landslide scarp points enclosed (percent)	Landslide scarp points enclosed within increment (number)	Area within increment (km²)	Landslide points within increment (percent)	Incremental Landslide density (scarps/km²)
Very High	≤ 0.87	75	27370	232	75	118
High	≤ 0.97	90	5474	108	15	51
Moderate	≤ 1.05	95	1825	68	5	27
Low	> 1.05	100	1824	610	5	3
Total	$0 < F_3 \leq 10$	100	36493	1018	100	36

741

Figure 13. Graph of true positive rate versus false positive rate for pre-Hurricane María susceptibility models across the study area tiles tested against head-scarp points (Hughes et al. 2019) and source polygons for Lares (Einbund et al. 2021b), Naranjito (Baxstrom et al. 2021a), and Utuado (Einbund et al. 2021a) with confusion matrix and formulas defining true positive rate (TPR) and false positive rate (FPR). Double-headed arrow indicates distance from ideal point (d_{IP}) for Naranjito source polygons and F_3 computed using NDSD soil depth. True positive rates are based on minimum value of the quasi-3D factor of safety, F_3, within the mapped source polygons or within a 3-m radius of the scarp points. Results for scarp points cover the final pre-Hurricane María susceptibility maps of Lares, Utuado, and Naranjito municipalities. Results for the landslide source polygons cover parts of the component tiles (Fig. 1). Landslide source mapping for Lares and Utuado (Einbund et al. 2021a, b) are near LAR and UTU (LAR2, UTU2, Fig. 1b). The graph compares F_3 performance based on the modified nonlinear area- and slope-dependent (NASD, modified from Pelletier and Rasmussen 2009) soil-depth model and two alternates: constant depth of 1.4 m, and the nonlinear depth- and slope-dependent soil-depth model (NDSD, Pelletier and Rasmussen 2009), with strength parameters and other inputs held constant. AUC denotes area under the curve of TPR versus FPR, N_p is the number of landslide source polygons, and N_{Sc} is the number of scarp points.

5 Discussion

Our analyses presented in the previous section (Sect. 4.6) indicate that the landslide susceptibility assessment successfully identifies areas where high percentages of Hurricane María landslides occurred. In succeeding paragraphs, we discuss some of the strengths, limitations, and unexpected findings of our approach and results.

Optimum ranges of internal friction angles for all three terranes (Fig. 5) are higher than commonly reported, but consistent with measured values of ϕ' for low normal stress (Likos et al. 2010). Most reported values of ϕ' for soils like those in the study area range from 17° to 41° as noted previously (Sec. 3.2) and are usually based on tests at normal stress greater than 100 kPa. In contrast, samples collected at two field monitoring sites tested at low and moderate normal stresses (Smith et al. 2020) using equipment and procedures described by Likos et al. (2010) had high friction angles for low normal stress. Smith et al. (2020) reported $\phi' = 34.8° - 35.5°$ ($c' = 0 - 4.4$ kPa) for two samples tested at effective normal stress, σ'_n, less than 120 kPa, $\phi' = 45.6°$ for a sample tested at $\sigma'_n \leq 30$ kPa, and $\phi' = 53.9°$ for another sample tested at $\sigma'_n, \leq 7$ kPa. Significantly, shear stress was considerably higher than normal stress for nearly all individual tests at $\sigma'_n \leq 15$ kPa, and many at $\sigma'_n \leq 30$, consistent with $\phi' > 45°$ at low normal stress. In addition to evidence for high internal friction angles at low normal stress, which is particularly relevant to abundant thin (< 0.5 m) landslides in Utuado, three other factors could contribute to stability and reduce the magnitude of ϕ' required to explain stability during dry conditions: (1) Soil suction measured at the sites between rainfall (Smith et al. 2020) indicates that suction stress probably contributes to stability. Preliminary tests indicate that considering modest amounts of suction stress (less than a few tens of kilopascals) during dry conditions in the analysis depicted by Fig. 5 shifts the cells having high TPR toward lower ranges of ϕ'. For example, increasing initial suction stress by -1 kPa shifts the optimum range of ϕ' to 35° – 40° for the submarine basalt and chert landslides compared to the 45° – 50° range in Fig. 5d. (2) Root resistance also likely contributes to slope stability to depths of about 0.5 – 0.6 m. Due to high annual rainfall, vegetation in the study areas tends to be shallow-rooted so that significant root resistance would decline rapidly below about 0.4 – 1.1 m depth (Simon et al. 1990; Larsen 2012). (3) Lateral stress variation also contributes to slope stability. Even in quasi-3D limit-equilibrium as used in computing F_3, combined resistance of neighboring grid cells (columns) and toe wedge contributes to stability and reduces the values of ϕ' and (or) c' needed to achieve stability of a potential landslide under dry conditions (Tables 2 and 3).

Our modelling workflow makes a few trade-offs to create a relatively conservative map of potential landslide sources that accounts for uncertainties. These trade-offs are between speed and simplicity of the assessment, statistical accuracy, and continuity of susceptibility zones. Some of the modelling steps (soil depth and F_3) add complexity, increase time needed to model susceptibility, and slightly reduce performance metrics (AUC and d_{IP}) compared to F_1 with constant soil depth. In exchange, soil depth and F_3 create more continuous susceptibility zones, join neighboring groups of high-susceptibility pixels, and eliminate isolated, commonly errant, pixels of high landslide susceptibility (Fig. 10 and 11). The increased continuity of the susceptibility zones makes them easier to implement in land use and emergency management. In addition, the potential source areas delineated on the map by the high and very high susceptibility areas provide areas susceptible to shallow landslides for estimating potential landslide runout and debris-flow inundation (Brien et al. 2021). Much of the reduction in AUC for F_3 results from using the minimum factor of

792   safety value computed for any trial landslide that includes a grid cell. Consequently, very high and high susceptibility

793   zones for F_3 are broader than for F_1 and thereby have a buffer along their edges. Nevertheless, as indicated by various

794   performance metrics and landslide densities in the susceptibility classes, the landslide assessment successfully

795   distinguishes areas having different levels of susceptibility to landslide initiation (Tables 3, 4) despite these trade-offs.

796   Although F_1 for constant depth has slightly better performance metrics (the highest AUC and smallest d_{IP}) than F_1 for

797   any of the soil depth models calibrated to landslide source depths (Table 2, Fig. 12a) at NAR, its performance metrics

798   are comparable to the nonlinear soil-depth models elsewhere. Our field observations indicate that depth of shallow,

799   rainfall-induced landslides is well correlated to depth of mobile regolith ("soil") due to strength and permeability

800   contrasts at its base. Soil-depth models represent the distribution of soil depth more consistently with field conditions

801   than constant depth in many settings (Pelletier and Rasmussen 2009; Ho et al. 2012; Catani et al. 2010; Nicótina et al.

802   2011; Gomes et al. 2016; Patton et al. 2018). Performance metrics (ED = $\sqrt{2}$; mean-squared error, MSE = σ_o^2) indicate

803   average depth was a poorer predictor of observed landslide depth than any of the models Tello (2020) tested for

804   Utuado. Despite odd differences in how the models estimate soil depth on mid-slope benches and flat valley bottoms,

805   the models we tested (NASD, NSDA, NDSD, LASD) predict thinner soils on ridge crests and thicker soils in hillside

806   hollows, consistent with patterns observed in Puerto Rico and elsewhere for dissected topography (Roering 2008). For

807   example, mean depths of landslide sources from field mapping in Puerto Rico were 3.25 m (for concave slopes), 2.5

808   m (for convex slopes), 2.7 m (for planar slopes; Schulz et al. 2023). The unexpected, good performance of F_1 for

809   constant soil depth at NAR points out limitations of soil depth models and may result in part from widespread

810   modifications to the landscape resulting from agriculture, road (e.g., Ramos-Scharrón et al. 2021) and building

811   construction, and other activities. Effects of these activities may have influenced the locations of shallow landslides

812   sufficiently to weaken correlation between landslide location and topographic features that influence soil depth (as at

813   LAR and ANA, Fig. 8a). The high degree of slope modification (roads and terraces) in the NAR calibration area is

814   likely a determining factor in F_1 performance there (Fig. 10). Identifying specific areas or features where constant-

815   depth F_1 classifies susceptibility differently than F_1 with other soil-depth models might reveal potential improvements.

816   Computing F_1 using the modified NASD soil-depth model resulted in the areas assigned to the moderate, high, and

817   very high susceptibility classes being more clearly delineated with little or no loss of performance compared to using

818   constant depth. The susceptibility zones in the constant-depth F_1 susceptibility map (Fig. 10b) are more diffuse or

819   fragmented (less continuous) than for the NASD soil depth (Fig. 10a) and other soil models we tested. Fragmentation

820   also occurred for susceptibility zones defined by slope categories (Fig. S3a). As noted previously, this improved

821   delineation came with only a slight reduction in AUC (0.88 to 0.86) and small increase in d_{IP} (0.26 to 0.30) for NAR.

822   When applied to the entire DEM tile covering Naranjito municipality, performance of F_1 for constant depth and F_1 for

823   NASD tied with each other and with slope categories (AUC = 0.87, d_{IP} = 0.29 - 0.30). As noted previously, when

824   checked against detailed source mapping, the performance metrics for F_3 are better than when compared against the

825   scarp points (Fig. 13). In addition, differences in performance metrics between constant depth and the NDSD model

826   and modified NASD model are negligible.

827   Other things being equal, the quasi-3D stability analysis, F_3, has a somewhat smaller AUC and larger d_{IP}, compared

828   to F_1 (Tables 2 and 3), but improves the final map. The improvements are better separation between the different

Natural Hazards
and Earth System
Sciences
Discussions
Open Access
EGU

829   susceptibility classes (Fig. 10 and 11) and a slightly more conservative map compared to F_1, which is helpful for life-
830   safety based land use planning and emergency response scenarios. With AUC=0.80 and d_{IP}=0.38 for F_3 based on the
831   modified NASD soil-depth and 3.5 m radius for the trial surface (Table 3), F_3 successfully identifies potential landslide
832   sources at NAR. For the entire map area, the AUC (0.84) and d_{IP} (0.33) scores are slightly better (Table 4, Fig. 13),
833   due in part to the large area of low landslide susceptibility that is underlain by limey sediments and characterized by
834   cone karst. By considering slope stability at the scale of representative landslide sources (median area, Fig. 3c), F_3
835   eliminates isolated grid cells and tiny clusters of 2 – 4 cells that likely are classified incorrectly by F_1 as highly or very
836   highly susceptible due to locally steep slopes at the pixel scale (1 m). Such isolated cells and clusters could be
837   eliminated after analysis, but boundaries of susceptible areas would remain somewhat ragged. In contrast our approach
838   provides an objective method for eliminating the isolated pixels and smoothing the boundaries. F_3 bridges gaps
839   between neighboring areas of low F_1 and thereby maps susceptible areas that are more continuous and with smoother,
840   more definite boundaries than F_1. Thus, F_3 further improves delineation of susceptible areas beyond improvements
841   achieved by using the modified NASD soil-depth model with F_1. Maps having continuous, clearly delineated areas
842   assigned to each susceptibility class such as those obtained by using F_3 reduce guesswork in making land use and
843   emergency management decisions by eliminating the ragged, transitional boundaries obtained with F_1. For example,
844   to compare the insets in Figs. 10 and 11 to each other as well as slope categories (Fig. S3a) and F_3 based on the NDSD
845   soil-depth model (Fig. S3d), see Fig. S3b, c, e and f. Well-defined potential landslide source areas also allow
846   estimation of areas susceptible to potential downslope runout and downstream inundation (Brien et al. 2021).
847   Performance metrics for F_3 considering detailed source mapping (Fig. 13) are sufficiently high ($0.85 \leq$ AUC ≤ 0.88)
848   to consider F_3 a very successful indicator of landslide susceptibility in our study area. As the basis for our final
849   susceptibility maps, we selected the F_3 map derived from the modified NASD soil depth model (Fig. 11a) because of
850   its high AUC combined with its well-defined source areas and the realistic modeled soil depths for estimating potential
851   landslide volumes. Model input parameters for the final maps are summarized in Supplemental Figures S1 and S2.
852   The susceptibility analysis portrayed in Fig. 11 and our final maps (Supplemental Figures S1 and S2) are valid
853   throughout the three municipalities despite the variable density of Hurricane María landslides throughout the map area
854   (Bessette-Kirton et al. 2017; Hughes et al. 2019) and within each susceptibility class. High landslide density generally
855   corresponds to low F_3 (Table 4); however, not all susceptible areas were equally affected by Hurricane María. Thus,
856   although some areas of low F_3, particularly in Naranjito, had low landslide density, the low density does not invalidate
857   the susceptibility assessment of the potential for future landslides. Factors such as antecedent soil moisture are known
858   to have affected the density of landslides induced by Hurricane María (Bessette-Kirton et al. 2019a) and were
859   addressed in the statistically based island-wide landslide susceptibility assessment of Hughes and Schulz (2020a).
860   Notably Naranjito had much lower root-zone soil moisture immediately after the hurricane than Utuado and Lares
861   (Fig. 26 of Hughes and Schulz 2020a). Variable rainfall intensity and duration are also known to affect landslide
862   response of susceptible areas (Larsen and Simon 1993; Pando et al. 2005). Intensity and duration are known to have
863   varied during Hurricane María, causing further differences in landslide density. Our assessment considered fully
864   saturated conditions with the water table at the ground surface to depict likely wettest-case soil moisture effects,
865   including high antecedent soil wetness, as well as high intensity and long-duration rainfall. Thus, it was not necessary

866   to specifically model antecedent soil moisture conditions. Less-severe conditions may produce landslides in the same

867   general areas as predicted by our assessment, however, in lower numbers than observed following Hurricane María.

868   Setting the boundaries between susceptibility classes based on F_1 or F_3 corresponding to specific values of TPR rather

869   than setting boundaries based on theoretical values of F_1 or F_3 (such as $F_3 = 1.0$) reduces uncertainty and ensures

870   correspondence between landslide density and degree of landslide susceptibility. Soil, saprolite, and bedrock are

871   inherently heterogenous. Their hydraulic and strength properties (and corresponding parameters) vary spatially at all

872   scales (Terzaghi et al. 1996). Other studies have applied probabilistic approaches and sensitivity analyses have been

873   applied successfully to address parameter uncertainty and improve accuracy of physically based modelling of landslide

874   susceptibility (Raia et al. 2014; Zieher et al. 2017; Canli et al. 2018). Many parameter combinations (c' and ϕ') can

875   achieve similar levels of predictive accuracy in computing F_1 for observed distributions of landslide slope and depth

876   (Baum et al. 2019; Baum 2021). These and other uncertainties such as transient pore-water pressures, subsurface

877   features, heterogeneity, and other factors, weaken the link between theoretical values of F_1 or F_3 and estimated

878   likelihood of failure for site-specific cases when applying limit-equilibrium slope stability analysis over wide areas.

879   On the other hand, maps classified based on TPR have a strong link to susceptibility. Such maps are readily comparable

880   to each other when F_1 or F_3 values are computed with different parameters, as they show like outcomes (areas that

881   capture 75%, 90% and 95% of observed landslides in this study). Comparing like outcomes focuses on differences

882   and uncertainties that affect the quality of the susceptibility assessment that might be masked by comparing the maps

883   when classified using the same F_1 or F_3 values. In this study, low values of F_1 and F_3 correspond to high observed

884   Hurricane María landslide density (Table 4), as would be expected. The selected boundaries for susceptibility classes

885   ensure a meaningful distinction between average landslide density in the successive classes (Table 4).

886   The susceptibility map correctly predicts locations of most landslides that are deeper than 3 m, despite the maximum

887   modeled soil depth of 3 m more typical of shallow landslides. Ten of the landslides summarized in Fig. 3e are deeper

888   than 3 m. Most (nine) are within the Naranjito tile (Fig. 1), and the other is in Lares. The mapped point on each

889   landslide headscarp and adjoining or surrounding slope was within the high or very high susceptibility zone for seven

890   of the ten deep landslides. The other three had head scarps on a gently sloping area (road or pad) that was set back a

891   few meters from the steep slope, but the adjoining slope with the landslide body was within the high and very high

892   susceptibility zones. Although the predicted locations might be right for the wrong reason (predicting a shallow

893   translational landslide rather than a deeper, translational, or rotational landslide), it is nevertheless encouraging that

894   the locations of even the deep landslides are identified for the sake of hazard assessment and planning. This probably

895   occurred because the deep landslides occurred well within the same slope range as other mapped landslides (Fig. 3,

896   4).

897   Despite the simplicity of soil and water parameters, the maps successfully predicted the effects from Hurricane María.

898   Calibrating with field data from the small calibration areas (ANA, LAR, UTU, and NAR, Fig. 1) and then testing with

899   the island-wide scarp points (Hughes et al. 2019) confirmed the successes of our approach (Supplemental Figures S1

900   and S2). Testing with detailed landslide source maps (Baxstrom et al. 2021a; Einbund et al. 2021a, 2021b) strengthens

901   our results even though they cover only a fraction of the study area.

902   The workflow outlined in Fig. 6 can be simplified in areas where few data are available. An accurate digital elevation

903   model and accurate landslide inventory with measurements of source area size, depth, and slope (Fig. 3) are the most

904   critical data for a landslide susceptibility analysis. Strength parameter ranges can be estimated from landslide source

905   depth and slope (Fig. 4, 5). Soil model calibration can be bypassed by assuming constant average landslide source

906   depth. Strength parameters can then be refined using the procedure described in Sect. 3.5. Alternately a soil model

907   and strength parameters can be calibrated simultaneously to the inventory as we did for the NAR calibration area.

908   Calculation of pressure head, F_1 and F_3 can then proceed as outlined in Sect. 3.4.2, 3.4.3, 3.4.4, and 3.9, followed by

909   validation and evaluation (Sect. 3.11). Compared to a map based on the simplest of landslide susceptibility approach,

910   slope ranges with its ragged, fragmented susceptibility zones, our procedure creates cohesive landslide susceptibility

911   zones that have smooth, buffered boundaries with only a slightly lower AUC score (0.84) than for slope (0.87) across

912   the entire study area.

913   **6 Conclusions**

914   We defined a workflow for assessing landslide susceptibility using multiple modelling stages and successfully applied

915   it using high-resolution (1-m) topography over a large (about 1000 km^2) geographic area in the central mountains of

916   Puerto Rico (Fig. 1). The workflow includes modelling soil depth, pressure head, and limit-equilibrium slope stability

917   (Fig. 6). Although calibration studies showed that assuming constant average soil depth as input for 1D (infinite-slope)

918   factor of safety against landsliding, F_1, gave the best performance metrics in a 2.5 km^2 calibration area, use of a soil-

919   depth model more clearly delineated areas susceptible to landslide initiation with only a modest reduction in the AUC

920   from 0.88 to 0.86. Using a quasi-3D limit-equilibrium slope stability analysis, the factor of safety, F_3, further refined

921   the susceptibility assessment by more clearly delineating boundaries between the different susceptibility classes and

922   by assessing stability at the scale of the observed median-sized landslides. Despite further reduction in AUC to 0.80

923   for the NAR calibration area, the map based on F_3 is more readily usable in certain applications than a map based on

924   F_1, and it still performs well as a classifier of landslide susceptibility. Performance metrics for the F_3 map of the entire

925   ~1000 km^2 study area, AUC = 0.84 and d_{IP} = 0.34, are slightly better than results at the NAR calibration area.

926   Performance measured against detailed source mapping of selected areas is even better: $0.85 \leq$ AUC ≤ 0.88 and 0.27

927    $\leq d_{IP} \leq 0.33$. These metrics indicate the map is suitable for planning, regulation, and emergency preparedness decisions

928   at the municipality scale. The map may also be used to assess hazards, such as ground collapse, resulting from landslide

929   initiation. Source area delineation as shown on maps may also be used for defining landslide starting locations and

930   surface area needed to assess areas with potential downslope movement of sediment mobilized by future landslides.

931   **Code availability**

932   Computer codes used in this study are available from the U.S. Geological Survey software repository as follows:

933   TRIGRS 2.1, https://doi.org/10.5066/F7M044QS; REGOLITH, https://doi.org/10.5066/P9U2RDWJ; and Slabs3D,

934   https://doi.org/10.5066/P9G4I8IU.

Natural Hazards
and Earth System
Sciences
Discussions

Data availability

The pre-event (2015) and post-event (2018) lidar topographic data used in this study are available through the National Map at https://apps.nationalmap.gov/lidar-explorer/#/. Soil mapping databases used to estimate soil properties are available from the Natural Resources Conservation Service at https://www.nrcs.usda.gov/resources/data-and-reports/web-soil-survey. Other data are available from the U.S. Geological Survey ScienceBase digital repository as follows: Summaries of geotechnical data, https://doi.org/10.5066/P9UXTQ4B; model input and output raster grids and model parameter input files used to produce the large maps (Supplemental Figures S1 and S2), https://doi.org/10.5066/P9C1U0LP; Landslide head scarp points, https://doi.org/10.5066/P9BVMD74; landslide polygons, https://doi.org/10.5066/F7JD4VRF, https://doi.org/10.5066/P9GBGA4I, https://doi.org/10.5066/P9YYU7W1, https://doi.org/10.5066/P9EASZZ7, and https://doi.org/10.5066/P9ZNUR1P.

Author contribution

RB, WS, MR and DB planned the study. WS managed the project. MT carried out model calibrations. RB developed the model code, carried out the simulations, and computed the model performance statistics. DB, WS, MR, MT, and RB analyzed the data. RB wrote the manuscript draft; DB, MR, and WS reviewed and edited the manuscript.

Competing interests

The authors declare that they have no conflict of interest.

Disclaimer

Any use of trade, firm, or product names is for descriptive purposes only and does not imply endorsement by the U.S. Government.

Acknowledgements

Natural Hazards
and Earth System
Sciences
Open Access
Discussions
EGU

References

960 **References**

961 Aaron, J., McDougall, S., Moore, J.R., Coe, J.A., and Hungr, O.: The role of initial coherence and path materials in
962 the dynamics of three rock avalanche case histories, Geoenvironmental Disasters, 4, 5. https://doi.org/10.1186/s40677-
963 017-0070-4, 2017.

964 Alvioli, M., and Baum, R.L.: Parallelization of the TRIGRS model for rainfall-induced landslides using the message
965 passing interface. Environ. Modell. Softw. 81, 122–135. https://doi.org/10.1016/j.envsoft.2016.04.002, 2016.

966 ASTM International: D2487-17e1, Standard Practice for Classification of Soils for Engineering Purposes (Unified
967 Soil Classification System), https://doi.org/10.1520/D2487-17E01, 2020.

968 Baum, R.L.: Rapid sensitivity analysis for reducing uncertainty in landslide hazard assessments, in: Understanding
969 and Reducing Landslide Disaster Risk, edited by: Guzzetti, F., Mihalić Arbanas, S., Reichenbach, P., Sassa, K.,
970 Bobrowsky, P.T., and Takara, K., Springer, Cham, Switzerland, 329–335, https://doi.org/10.1007/978-3-030-60227-
971 7_37, 2021.

972 Baum, R.L.: Slabs3D—A Fortran 95 program for analyzing potential shallow landslides in a digital landscape, U.S.
973 Geol. Surv. software release [code], https://doi.org/10.5066/P9G4I8IU, 2023.

974 Baum, R.L., and Lewis, A.C.: Engineering soil classification and geotechnical measurements in Lares, Naranjito, and
975 Utuado, Puerto Rico: U.S. Geol. Surv. data release [data set], https://doi.org/10.5066/P9UXTQ4B, 2023.

976 Baum, R.L., Brien, D.L., Reid, M.E., Schulz, W.H., Tello, M.J., and Bedinger, E.C.: Model input and output data
977 covering Lares Municipio, Utuado Municipio, and Naranjito Municipio, Puerto Rico, for landslide initiation
978 susceptibility assessment after Hurricane Maria: U.S. Geol. Surv. data release [data set],
979 https://doi.org/10.5066/P9C1U0LP, 2023.

980 Baum, R.L., Savage, W.Z., and Godt, J.W.: TRIGRS—A Fortran program for transient rainfall infiltration and grid-
981 based regional slope-stability analysis, version 2.0, U.S. Geol. Surv. Open-File Report 2008-1159, 75 pp.
982 https://doi.org/10.3133/ofr20081159, 2008.

983 Baum, R.L., Godt, J.W., and Savage, W.Z.: Estimating the timing and location of shallow rainfall-induced landslides
984 using a model for transient, unsaturated infiltration. Journal of Geophysical Research: Earth Surface, 115(F3), F03013.
985 https://doi.org/10.1029/2009JF001321, 2010.

986 Baum, R.L., Godt, J.W., Coe, J.A., and Reid, M.E.: Assessment of shallow landslide potential using 1D and 3D slope
987 stability analysis, in: Landslides and Engineered Slopes: Protecting Society through Improved Understanding, edited
988 by: Eberhardt, E., Froese, C., Turner, A.K., and Leroueil, S., Taylor & Francis Group, London, pp. 1667–1672, ISBN
989 978-0-415-62123-6, 2012.

990 Baum, R.L., Schulz, W.H., Brien, D.L., Burns, W.L., Reid, M.E., and Godt, J.W.: Progress in regional landslide hazard
991 assessment—Examples from the USA, in: Landslide Science for a Safer Geoenvironment , edited by, Sassa, K.,
992 Canuti, P., and Yin, Y., Springer, Cham, Switzerland, pp. 21–36. https://doi.org/10.1007/978-3-319-04999-1_2, 2014.

993 Baum, R.L., Cerovski-Darriau, C., Schulz, W.H., Bessette-Kirton, E., Coe, J.A., Smith, J.B., and Smoczyk, G.M.:
994 Variability of hurricane María debris-flow source areas in Puerto Rico—Implications for hazard assessment, AGU
995 Fall Meeting, Washington, DC 2018, NH14A-02, https://agu.confex.com/agu/fm18/meetingapp.cgi/Paper/412740,
996 2018.

997 Baum, R.L., Scheevel, C.R., and Jones, E.S.: Constraining parameter uncertainty in modeling debris-flow initiation
998 during the September 2013 Colorado Front Range storm, in: Debris-flow Hazards Mitigation: Mechanics, Monitoring,
999 Modeling, and Assessment, edited by: Kean, J.W., Coe, J.A., Santi, P.M., and Guillen, B.K., Association of
1000 Environmental and Engineering , Brunswick, Ohio, pp. 249–256, https://doi.org/10.25676/11124/173212, 2019.

1001 Baum, R.L., Bedinger, E.C., and Tello, M.J.: REGOLITH--A Fortran 95 program for estimating soil mantle thickness
1002 in a digital landscape for landslide and debris-flow hazard assessment, U.S. Geol. Surv. software release [code],
1003 https://doi.org/10.5066/P9U2RDWJ, 2021.

1004 Bawiec, W.J.: Geologic terranes of Puerto Rico, in: Geology, geochemistry, geophysics, mineral occurrences, and
1005 mineral resource assessment for the commonwealth of Puerto Rico, edited by: Bawiec W.J., U.S. Geol. Surv. Open-
1006 File Rep. 98–38. https://doi.org/10.3133/ofr9838, 1998.

1007 Baxstrom, K.W., Einbund, M.M., and Schulz, W.H.: Map data from landslides triggered by Hurricane María in a
1008 section of Naranjito, Puerto Rico, U.S. Geol. Surv. data release [data set], https://doi.org/10.5066/P9GBGA4I, 2021a.

1009 Baxstrom, K.W., Einbund, M.M., and Schulz, W.H.: Map data from landslides triggered by Hurricane María in the
1010 greater karst region of northwest Puerto Rico, U.S. Geol. Surv. data release [data set],
1011 https://doi.org/10.5066/P9YYU7W1, 2021b.

1012 Begueria, S.: Validation and evaluation of predictive models in hazard assessment and risk management. Nat. Hazards,
1013 37, 315–329. https://doi.org/10.1007/s11069-005-5182-6, 2006.

1014 Benda, L., Miller, D., Andras, K., Bigelow, P., Reeves, G., and Michael, D.: NetMap: A new tool in support of
1015 watershed science and resource management, Forest Sci., 53(2), 206-219.
1016 https://doi.org/10.1093/forestscience/53.2.206, 2007.

1017 Bessette-Kirton, E.K., Coe, J.A., Godt, J.W., Kean, J.W., Rengers, F.K., Schulz, W.H., Baum, R.L., Jones, E.S., and
1018 Staley, D.M.: Map data showing concentration of landslides caused by hurricane María in Puerto Rico. U.S. Geol.
1019 Surv. data release [data set], https://doi.org/10.5066/F7JD4VRF, 2017.

1020 Bessette-Kirton, E.K., Cerovski-Darriau, C., Schulz, W.H., Coe, J.A., Kean, J.W., Godt, J.W., Thomas, M.A., and
1021 Hughes, K.S.: Landslides triggered by Hurricane María: Assessment of an extreme event in Puerto Rico, GSA Today,
1022 29, 4–10. https://doi.org/10.1130/GSATG383A.1, 2019a.

1023 Bessette-Kirton, E.K., Kean, J.W., Coe, J.A., Rengers, F.K., and Staley, D.M.: An evaluation of debris-flow runout
1024 model accuracy and complexity in Montecito, California: Towards a framework for regional inundation-hazard
1025 forecasting, in: Debris-flow Hazards Mitigation: Mechanics, Monitoring, Modeling, and Assessment, edited by: Kean,
1026 J.W., Coe, J.A., Santi, P.M., Guillen, B.K., Association of Environmental and Engineering Geologists, Brunswick,
1027 Ohio, pp. 257–264. https://doi.org/10.25676/11124/173211, 2019b.

1028 Bessette-Kirton, E.K., Coe, J.A., Kelly, M.A., Cerovski-Darriau, C., and Schulz, W.H.: Map data from landslides
1029 triggered by Hurricane María in four study areas of Puerto Rico. U.S. Geol. Surv. data release [data set].
1030 https://doi.org/10.5066/P9OW4SLX, 2019c.

1031 Bessette-Kirton, E.K., Coe, J.A., Schulz, W.H., Cerovski-Darriau, C., and Einbund, M.M.: Mobility characteristics of
1032 debris slides and flows triggered by Hurricane María in Puerto Rico, Landslides 17, 2795–2809,
1033 https://doi.org/10.1007/s10346-020-01445-z, 2020.

1034   Brien, D.L., Reid, M.E., Cronkite-Ratcliff, C., and Perkins, J.P.: Portraying runout and inundation from hurricane-
1035   induced landslides in Puerto Rico, Geological Society of America Abstracts with Programs. 53(6), 85-4,
1036   https://doi.org/10.1130/abs/2021AM-368632, 2021.

1037   Catani, F., Segoni, S., and Falorni, G.: An empirical geomorphology-based approach to the spatial prediction of soil
1038   thickness at catchment scale, Water Resour. Res., 46(5), W05508, https://doi.org/10.1029/2008WR007450, 2010.

1039   Canli, E., Mergili, M., Thiebes, B., and Glade, T.: Probabilistic landslide ensemble prediction systems: Lessons to be
1040   learned from hydrology, Nat. Hazard. Earth Sys., 18(8), 2183–2202, https://doi.org/10.5194/nhess-18-2183-2018,
1041   2018.

1042   Carrara, A., Guzzetti, F., Cardinali, M., and Reichenbach, P.: Use of GIS technology in the prediction and monitoring
1043   of landslide hazard, Nat. Hazards, 20, 117–135, https://doi.org/10.1023/A:1008097111310, 1999.

1044   Chung, C.F., and Fabbri, A.G.: Validation of spatial prediction models for landslide hazard mapping, Nat. Hazards,
1045   30, 451–472, https://doi.org/10.1023/B:NHAZ.0000007172.62651.2b, 2003.

1046   Einbund, M.M., Baxstrom, K.S., and Schulz, W.H.: Map data from landslides triggered by Hurricane María in four
1047   study areas in the Utuado municipality, Puerto Rico, U.S. Geol. Surv. data release [data set],
1048   https://doi.org/10.5066/P9ZNUR1P, 2021a.

1049   Einbund, M.M., Baxstrom, K.S., and Schulz, W.H.: Map data from landslides triggered by Hurricane María in four
1050   study areas in the Lares municipality, Puerto Rico. U.S. Geol. Surv. data release [data set],
1051   https://doi.org/10.5066/P9EASZZ7, 2021b.

1052   Ellen, S.D., Mark, R.K., Cannon, S.H., and Knifong, D.L.: Map of debris-flow hazard in the Honolulu District of
1053   Oahu, Hawaii, U.S. Geol. Surv. Open-File Rep. 93-213, 28 pp., https://doi.org/10.3133/ofr93213, 1993.

1054   Fan, L., Lehmann, P., McArdell, B., and Or, D.: Linking rainfall-induced landslides with debris flows runout patterns
1055   towards   catchment   scale   hazard   assessment,   Geomorphology   280,   1-15.
1056   https://doi.org/10.1016/j.geomorph.2016.10.007, 2017.

1057   Fawcett, T.: An   introduction   to   ROC   analysis,   Pattern   Recogn.   Lett.,   27(8),   861–874,
1058   https://doi.org/10.1016/j.patrec.2005.10.010, 2006.

1059   George, D.L., and Iverson, R.M.: A depth-averaged debris-flow model that includes the effects of evolving dilatancy:
1060   2. Numerical   predictions   and   experimental   tests,   P.   Roy.   Soc.   A-Math.   Phy.,   470(2170),   20130820,
1061   https://doi.org/10.1098/rspa.2013.0820, 2014.

1062   Godt, J.W., Schulz, W.H., Baum, R.L., and Savage, W.Z.: Modeling rainfall conditions for shallow landsliding in
1063   Seattle, Washington, in: Landslides and Engineering Geology of the Seattle, Washington, Area, edited by: Baum,
1064   R.L.,   Godt,   J.W.,   Highland,   L.M.,   Geological   Society   of   America,   Boulder,   Colorado,   137–152,
1065   https://doi.org/10.1130/2008.4020(08), 2008.

1066   Gomes, G.J.C., Vrugt, J.A., and Vargas, Jr., E.A.: Toward improved prediction of the bedrock depth underneath
1067   hillslopes: Bayesian inference of the bottom-up control hypothesis using high-resolution topographic data, Water
1068   Resour. Res., 52(4), 3085–3112, https://doi.org/10.1002/2015WR018147, 2016.

Natural Hazards
and Earth System
Sciences
Discussions

Gupta, H.V., Kling, H., Yilmaz, K.K., and Martinez, G.F.: Decomposition of the mean squared error and NSE performance criteria: Implications for improving hydrological modeling. J. Hydrol., 377(1-2), 80–91. https://doi.org/10.1016/j.jhydrol.2009.08.003, 2009.

Ho, J.-Y., Lee, K.T., Chang, T.-C., Wang, Z.-Y., and Liao, Y.-H.: Influences of spatial distribution of soil thickness on shallow landslide prediction. Eng. Geol., 124, 38–46. https://doi.org/10.1016/j.enggeo.2011.09.013, 2012.

Hovland, H.J.: Three-dimensional slope stability analysis method. J. Geotech. Eng.-ASCE, 103(GT9), 971–986. https://doi.org/10.1061/AJGEB6.0000493, 1977.

Hsu, Y.C., and Liu, K.F.: Combining TRIGRS and DEBRIS-2D models for the simulation of a rainfall infiltration induced shallow landslide and subsequent debris flow, Water, 11(5), 890, https://doi.org/10.3390/w11050890, 2019.

Hughes, K.S., Bayouth-García, D., Martínez-Milian, G.O., Schulz, W.H., and Baum, R.L.: Map of slope-failure locations in Puerto Rico after Hurricane María. U.S. Geol. Surv. data release [data set], https://doi.org/10.5066/P9BVMD74, 2019.

Hughes, K.S., and Schulz, W.H.: Map depicting susceptibility to landslides triggered by intense rainfall, Puerto Rico, U.S. Geol. Surv. Open-File Rep. 2020–1022, 91 pp., 1 plate, scale 1:150,000. https://doi.org/10.3133/ofr20201022, 2020a.

Hughes, K.S., Schulz, W.H.: Results from frequency-ratio analyses of soil classification and land use related to landslide locations in Puerto Rico following Hurricane María. U.S. Geol. Surv. data release [data set], https://doi.org/10.5066/P9VK2FAL, 2020b.

Hungr, O., Salgado, F.M., and Byrne, P.M.: Evaluation of a three-dimensional method of slope-stability analysis, Can. Geotech. J., 26(4), 679–686, https://doi.org/10.1139/t89-079, 1989.

Iverson, R.M.: Landslide triggering by rain infiltration, Water Resour. Res., 36(7), 1897–1910, https://doi.org/10.1029/2000WR900090, 2000.

Jibson, R.W.: Debris flows in southern Puerto Rico, in: Landslide processes of the eastern United States and Puerto Rico, edited by: Schultz A.P., and Jibson R.W., Geol. S. Am. S., 236, 29–55, https://doi.org/10.1130/SPE236-p29, 1989.

Jolly, W.T., Lidiak, E.G., Dickin, A.P., and Wu, T.-W.: Geochemical diversity of Mesozoic island arc tectonic blocks in eastern Puerto Rico, in: Tectonics and Geochemistry of the Northeastern Caribbean, edited by: Likiak, E.G., Larue, D.K., Geol. S. Am. S., 322, 67–98, https://doi.org/10.1130/0-8137-2322-1.67, 1998.

Lambe, T.W., and Whitman, R.V.: Soil Mechanics, John Wiley & Sons, New York, 553 pp., ISBN 0471511927, 1969.

Larsen, M.C., and Torres-Sanchez, A.J.: Landslides triggered by hurricane Hugo in eastern Puerto Rico, September 1989. Caribb. J. Sci., 28(3-4), 113–125, 1992.

Larsen, M.C., and Simon, A.: A rainfall intensity-duration threshold for landslides in a humid-tropical environment, Puerto Rico, Geogr. Ann. A, 75(1-2), 13-23, https://doi.org/10.1080/04353676.1993.11880379, 1993.

Larsen, M.C., and Parks, J.E.: Map showing landslide susceptibility in the Comerio municipality, Puerto Rico, U.S. Geol. Surv. Open-File Rep. 98-566, 1 plate, scale 1:20,000. https://doi.org/10.3133/ofr98566, 1998.

Larsen, M.C., and Torres-Sanchez, A.J.: The frequency and distribution of recent landslides in three montane tropical regions of Puerto Rico, Geomorphology, 24(4), 309–331, https://doi.org/10.1016/S0169-555X(98)00023-3, 1998.

Natural Hazards
and Earth System
Sciences

Discussions

1106   Larsen M.C., Santiago, M., Jibson, R., and Questell, E.: Map showing susceptibility to rainfall-triggered landslides in

1107   the municipality of Ponce, Puerto Rico, U.S. Geol. Surv. Scientific Investigations Map 2818, 1 plate, scale 1:30,000,

1108   https://doi.org/10.3133/sim2818, 2004.

1109   Larsen, M.C.: Landslides and sediment budgets in four watersheds in eastern Puerto Rico, in: Water Quality and

1110   Landscape Processes of Four Watersheds in Eastern Puerto Rico, edited by: Murphy, S.F., and Stallard, R.F., U.S.

1111   Geol. Surv. Prof. Paper 1789, 153–178, https://doi.org/10.3133/pp1789, 2012.

1112   Lee, S., Ryu, J.-H., Min, K., and Won, J.-S.: Landslide susceptibility analysis using GIS and artificial neural network,

1113   Earth Surf. Proc. Land., 28(12), 1361–1376, https://doi.org/10.1002/esp.593, 2003.

1114   Lepore, C., Kamal, S.A., Shanahan, P., and Bras, R.L.: Rainfall-induced landslide susceptibility zonation of Puerto

1115   Rico, Environ. Earth Sci., 66, 1667–1681, https://doi.org/10.1007/s12665-011-0976-1, 2012.

1116   Lepore, C., Arnone, E., Noto, L.V., Sivandran, G., and Bras, R.L.: Physically based modeling of rainfall-triggered

1117   landslides: A case study in the Luquillo forest, Puerto Rico, Hydrol. Earth Syst. Sci., 17(9), 3371–3387,

1118   https://doi.org/10.5194/hess-17-3371-2013, 2013.

1119   Likos, W.J., Wayllace, A., Godt, J., and Lu, N.: Modified direct shear apparatus for unsaturated sands at low suction

1120   and stress, Geotech. Test. J., 33(4), 286–298, https://doi.org/10.1520/GTJ102927, 2010.

1121   Mergili, M., Schwarz, L., and Kociu, A.: Combining release and runout in statistical landslide susceptibility modeling,

1122   Landslides, 16(11), 2151–2165, https://doi.org/10.1007/s10346-019-01222-7, 2019.

1123   Murphy, S.F., Stallard, R.F., Larsen, M.C., and Gould, W.A.: Physiography, geology, and land cover of four

1124   watersheds in eastern Puerto Rico, U.S. Geol. Surv. Prof. Paper 1789-A, 24 pp., https://doi.org/10.3133/pp1789A,

1125   2012.

1126   Monroe, W.H.: The karst landforms of Puerto Rico, U.S. Geol. Surv. Prof. Paper 899, 69 pp.,

1127   https://doi.org/10.3133/pp899, 1976.

1128   Nicótina, L., Tarboton, D.G., Tesfa, T.K., and Rinaldo, A.: Hydrologic controls on equilibrium soil depths, Water

1129   Resour. Res., 47(4), W04517, https://doi.org/10.1029/2010WR009538, 2011.

1130   Pando, M.A., Ruiz, M.E., and Larsen, M.C.: Rainfall-induced landslides in Puerto Rico: An overview, in: Slopes and

1131   Retaining Structures Under Seismic and Static Conditions, edited by Gabr, M.A., Bowders, J.J., Elton, D., and

1132   Zornberg, J.G., ASCE Geotech. SP., 140, 2911–2925, https://doi.org/10.1061/40787(166)25, 2005.

1133   Patton, N.R., Lohse, K.A., Godsey, S.E., Crosby, B.T., and Seyfried, M.S.: Predicting soil thickness on soil mantled

1134   hillslopes, Nat. Commun., 9, 3329, https://doi.org/10.1038/s41467-018-05743-y, 2018.

1135   Pelletier, J.D., and Rasmussen, C.: Geomorphically based predictive mapping of soil thickness in upland watersheds,

1136   Water Resour. Res., 45(9):W09417. https://doi.org/10.1029/2008WR007319, 2009.

1137   Perkins, J.P., Baxstrom, K.W., Einbund, M.M, and Schulz, W.H: Modified basal contact of the Tertiary Lares

1138   Limestone in the vicinity of Utuado, Puerto Rico, USA, derived from USGS Open-File Report 98-038, U.S. Geol.

1139   Surv. data release [data set], https://doi.org/10.5066/P9NL9EZG, 2022.

1140   Raia, S., Alvioli, M., Rossi, M., Baum, R.L., Godt, J.W., and Guzzetti F.: Improving predictive power of physically

1141   based rainfall-induced shallow landslide models: A probabilistic approach, Geosci. Model Dev., 7(2), 495–514,

1142   https://doi.org/10.5194/gmd-7-495-2014, 2014.

1143 Ramos-Scharrón, C.E., Arima, E.Y., Guidry, A., Ruffe, D., and Vest B.: Sediment mobilization by hurricane-driven
1144 shallow landsliding in a wet subtropical watershed, J. Geophys. Res.-Earth, 126(5), e2020JF006054,
1145 https://doi.org/10.1029/2020JF006054, 2021.

1146 Reid, M.E., Christian, S.B., Brien, D.L., and Henderson, S.T.: Scoops3D—Software to analyze 3D slope stability
1147 throughout a digital landscape, U.S. Geol. Surv. Techniques and Methods 14-A1 [code], 218 pp.
1148 https://doi.org/10.3133/tm14A1, 2015.

1149 Reid, M.E., Coe, J.A., and Brien, D.L.: Forecasting inundation from debris flows that grow volumetrically during
1150 travel, with application to the Oregon coast range, USA, Geomorphology, 273, 396–411.
1151 https://doi.org/10.1016/j.geomorph.2016.07.039, 2016.

1152 Roering, J.J.: How well can hillslope evolution models "explain" topography? Geol. Soc. Am. Bull., 120(9-10), 1248–
1153 1262, https://doi.org/10.1130/B26283.1, 2008.

1154 Schulz, W.H., Jensen, E.K., Cerovski-Darriau, C.R., Baum, R.L., Thomas, M.A., and Coe, J.A.: Field observations of
1155 landslides and related materials following Hurricane Maria, Puerto Rico, U.S. Geol. Surv. data release [data set],
1156 https://doi.org/10.5066/P9T9KZ6T, 2023.

1157 Simon, A., Larsen, M.C., and Hupp, C.R.: The role of soil processes in determining mechanisms of slope failure and
1158 hillslope development in a humid-tropical forest eastern Puerto Rico, Geomorphology, 3(3-4), 263–286,
1159 https://doi.org/10.1016/0169-555X(90)90007-D, 1990.

1160 Smith, J.B., Thomas, M.A., Ashland, F., Michel, A.R., Wayllace, A., and Mirus, B.B.: Hillslope hydrologic
1161 monitoring data following Hurricane María in 2017, Puerto Rico, July 2018 to June 2020, U.S. Geol. Surv. data release
1162 [data set], https://doi.org/10.5066/P9548YK2, 2020.

1163 Soil Survey Staff: Soil Survey Geographic (SSURGO) Database for Puerto Rico, all regions. U.S. Department of
1164 Agriculture Natural Resources Conservation Service [data set], https://websoilsurvey.sc.egov.usda.gov/app/ (last
1165 access: 10 August 2023), 2018.

1166 Sowers, G.F.: Landslides in weathered volcanics in Puerto Rico, in: Proceedings of the Fourth Pan-American
1167 Conference on Soil Mechanics and Foundation Engineering, American Society of Civil Engineers, New York, 105–
1168 115, 1971.

1169 Taggart, B.E., and Joyce, J.: Radiometrically dated marine terraces on northwestern Puerto Rico, in: Transactions of
1170 the 12th Caribbean Geological Conference, St. Croix, U.S. Virgin Islands, August 7th-11th, 1989, Miami Geological
1171 Society, South Miami, Florida, 248–258, 1991.

1172 Taylor, D.W.: Fundamentals of Soil Mechanics, John Wiley & Sons, New York, 700 pp., 1948.

1173 Thomas, M.A, and Cerovski-Darriau, C.: Infiltration data collected post-Hurricane María across landslide source area
1174 materials, Puerto Rico, USA, U.S. Geol. Surv. data release [data set], https://doi.org/10.5066/P9SCGVF7, 2019.

1175 Tello, M.: Optimization of landslide susceptibility modeling: A Puerto Rico case study, Master of Science Thesis,
1176 Colorado School of Mines, Golden, Colorado, https://hdl.handle.net/11124/174137, 2020.

1177 Terzaghi, K., Peck, R.B., and Mesri, G.: Soil Mechanics in Engineering Practice, 3rd ed. John Wiley & Sons: New
1178 York, 549 pp., ISBN: 978-0-471-08658-1, 1996.

1179 Turnbull, W.J., and Hvorslev, M.J.: Special problems in slope stability, Journal of the Soil Mechanics and Foundations
1180 Division, 93(SM4), 499–528, https://doi.org/10.1061/JSFEAQ.0001004, 1967.
1181 U.S. Geological Survey: 2015–2016 USGS Puerto Rico LiDAR (project PR_PuertoRico_2015) [data set], at
1182 https://apps.nationalmap.gov/lidar-explorer/#/ (last access: 10 August 2023), 2018.
1183 U.S. Geological Survey: 2018 USGS Puerto Rico – Virgin Islands LiDAR (project PR_PRVI_A_2018),
1184 https://apps.nationalmap.gov/lidar-explorer/#/ (last access: 10 August 2023), 2020a.
1185 U.S. Geological Survey: 2018 USGS Puerto Rico – Virgin Islands LiDAR (project PR_PRVI_D_2018),
1186 https://apps.nationalmap.gov/lidar-explorer/#/ (last access: 10 August 2023), 2020b.
1187 U.S. Geological Survey: 2018 USGS Puerto Rico – Virgin Islands LiDAR (project PR_PRVI_H_2018),
1188 https://apps.nationalmap.gov/lidar-explorer/#/ (last access: 10 August 2023), 2020c.
1189 Zieher, T., Rutzinger, M., Schneider-Muntau, B., Perzl, F., Leidinger, D., Formayer, H., and Geitner, C.: Sensitivity
1190 analysis and calibration of a dynamic physically based slope stability model, Nat. Hazard. Earth Sys., 17(6), 971–992.
1191 https://doi.org/10.5194/nhess-17-971-2017, 2017.
1192